Stress and flux reconstruction in Biot's poro-elasticity problem with application to a posteriori error analysis

Rita Riedlbeck, Daniele Di Pietro, Alexandre Ern, Sylvie Granet, Kyrylo Kazymyrenko

Stress and flux reconstruction in Biot's poro-elasticity problem with application to a posteriori error analysis

Rita Riedlbeck*,[1,3], Daniele A. Di Pietro[1], Alexandre Ern[2], Sylvie Granet[3], and Kyrylo Kazymyrenko[3]

[1]University of Montpellier, Institut Montpelliérain Alexander Grothendieck, 34095 Montpellier CEDEX 5, France
[2]University Paris-Est, CERMICS (ENPC), 6-8 avenue Blaise Pascal, 77455 Marne-la-Vallée CEDEX 2, France
[3]EDF R&D, IMSIA, 7 boulevard Gaspard Monge, 91120 Palaiseau, France

February 20, 2017

Abstract

We derive equilibrated reconstructions of the Darcy velocity and of the total stress tensor for Biot's poro-elasticity problem. Both reconstructions are obtained from mixed finite element solutions of local Neumann problems posed over patches of elements around mesh vertices. The Darcy velocity is reconstructed using Raviart–Thomas finite elements and the stress tensor using Arnold–Winther finite elements so that the reconstructed stress tensor is symmetric. Both reconstructions have continuous normal component across mesh interfaces. Using these reconstructions, we derive a posteriori error estimators for Biot's poro-elasticity problem, and we devise an adaptive space-time algorithm driven by these estimators. The algorithm is illustrated on test cases with analytical solution, on the quarter five-spot problem, and on an industrial test case simulating the excavation of two galleries.

Key words: a posteriori error estimate; equilibrated stress reconstruction; Arnold-Winther finite element space; Biot's poro-elasticity problem

1 Introduction

Biot's poro-elasticity problem was originally proposed by von Terzaghi [40] and Biot [6] to describe the hydro-mechanical coupling between the displacement field $\underline{u}$ of a linearly elastic, porous material and the pressure p of an incompressible, viscous fluid saturating its pores. Let $\Omega \subset \mathbb{R}^2$ be the simply connected polygonal region occupied by the porous material, and let $t_F > 0$ denote the simulation time. For the sake of simplicity, we assume that the material is clamped at its impermeable boundary, and fix the Biot–Willis coefficient equal to 1. We also assume that the deformation of the material is much slower than the flow rate, so that the problem can be considered in quasi-static form. Then, the displacement field $\underline{u} : \Omega \times (0, t_F) \to \mathbb{R}^2$

*Corresponding author, rita.riedlbeck@edf.fr

and the pore pressure $p : \Omega \times (0, t_F) \to \mathbb{R}$ are determined by

$$-\underline{\nabla} \cdot \underline{\underline{\sigma}}(\underline{u}) + \underline{\nabla} p = \underline{f} \qquad \text{in } \Omega \times (0, t_F), \tag{1.1a}$$

$$\partial_t(\nabla \cdot \underline{u} + c_0 p) - \nabla \cdot (\kappa \underline{\nabla} p) = g \qquad \text{in } \Omega \times (0, t_F), \tag{1.1b}$$

$$\underline{u} = \underline{0} \qquad \text{on } \partial\Omega \times (0, t_F), \tag{1.1c}$$

$$\kappa \underline{\nabla} p \cdot \underline{n}_\Omega = 0 \qquad \text{on } \partial\Omega \times (0, t_F), \tag{1.1d}$$

$$\underline{u}(\cdot, 0) = \underline{u}_0 \qquad \text{in } \Omega, \tag{1.1e}$$

where $\underline{f}$ denotes the volumetric body force acting on the material, g a volumetric fluid source (which, if $c_0 = 0$, is assumed to verify the compatibility condition $\int_\Omega g(\underline{x}, t) \mathrm{d}\underline{x} = 0$ for each $t \in (0, t_F)$), and the effective stress tensor $\underline{\underline{\sigma}}$ is linked to the strain tensor $\underline{\underline{\epsilon}}$ through Hooke's law

$$\underline{\underline{\sigma}}(\underline{u}) = 2\mu \underline{\underline{\epsilon}}(\underline{u}) + \lambda \mathrm{tr}(\underline{\underline{\epsilon}}(\underline{u})) \underline{\underline{I}}_2, \qquad \underline{\underline{\epsilon}}(\underline{u}) = \frac{1}{2}(\underline{\underline{\nabla}} \underline{u} + \underline{\underline{\nabla}} \underline{u}^{\mathrm{T}}), \tag{1.2}$$

where $\underline{\underline{I}}_2$ is the two-dimensional identity matrix. The Lamé parameters λ and μ, describing the mechanical properties of the material, are assumed such that $\mu > 0$ and $\lambda + \frac{2}{3}\mu > 0$ uniformly in Ω. The scalar field $\kappa : \Omega \to \mathbb{R}$ describes the mobility of the fluid and we assume that there exist positive real numbers $\kappa_\flat$ and $\kappa_\sharp$ such that $\kappa_\flat \le \kappa \le \kappa_\sharp$ a.e. in Ω. When the specific storage coefficient c_0 is zero, we enforce uniqueness of the pore-pressure in (1.1) by further requiring that

$$\int_\Omega p(\cdot, t) \mathrm{d}\underline{x} = 0 \qquad \text{in } (0, t_F). \tag{1.3}$$

On the other hand, for $c_0 > 0$, we complement (1.1) by the following initial condition on the pressure:

$$p(\cdot, 0) = p_0 \qquad \text{in } \Omega. \tag{1.4}$$

In practice, even when $c_0 = 0$, the initial velocity field $\underline{u}_0$ in (1.1e) is usually obtained by first setting p_0 equal to the solution of a hydrostatic computation and then calculating $\underline{u}_0$ by solving (1.1a) with $p = p_0$ (cf. Remark 2.1 in [33]). The well-posedness of Biot's consolidation problem has been analyzed in [38, 41]. A suitable approximation method consists of using Taylor–Hood H^1-conforming finite elements in space (using piecewise polynomials of order $k \ge 1$ for the pressure and of order $(k+1)$ for the displacement) and a backward Euler scheme in time. The corresponding a priori error analysis can be found in [28–30]. This discretization strategy is adopted in the `Code_Aster`[1] software, which is used for the numerical examples presented in this work. Several other discretization methods have been studied in the literature, among which we cite, in particular, the fully coupled algorithm of [7], where the Hybrid High-Order method of [12] is used for the elasticity operator, while the weighted discontinuous Galerkin method of [13] is used for the Darcy operator.

The two governing equations (1.1a) and (1.1b) express, respectively, the conservation of mechanical momentum and fluid mass. In particular, the Darcy velocity $\underline{\phi}(p) := -\kappa \underline{\nabla} p$ and the total stress tensor $\underline{\underline{\theta}}(\underline{u}, p) := \underline{\underline{\sigma}}(\underline{u}) - p \underline{\underline{I}}_2$ have continuous normal component across any interface in the domain Ω, and the divergence of these fields is locally in equilibrium with the sources (and the accumulation terms) in any control volume. It is well known that the use of H^1-conforming finite elements does not lead to discrete fluxes $\underline{\phi}(p_h^n)$ and $\underline{\underline{\theta}}(\underline{u}_h^n, p_h^n)$ (where $(\underline{u}_h^n, p_h^n)$ denotes the discrete solution at a given discrete time t^n) that satisfy the discrete counterpart of the above properties across mesh interfaces and in mesh cells. The first contribution of this work is to fill this gap by reconstructing equilibrated fluxes from local mixed finite element solves on cell

[1] `http://web-code-aster.org`

patches around mesh vertices. The Darcy velocity reconstruction uses, as in [9,11,21], Raviart–Thomas mixed finite elements [35] on cell patches around vertices of the original mesh. The construction we propose for the total stress tensor is, to our knowledge, novel and is based on the use of the Arnold–Winther mixed finite element [4], again on the same vertex-based cell patches. This construction provides, in particular, a symmetric total stress tensor. The Darcy velocity and the total stress tensor are reconstructed at each discrete time, they have continuous normal component across any mesh interface, and their divergence is locally in equilibrium with the sources (averaged over the time interval) in any mesh cell. In steady-state linear elasticity, element-wise (as opposed to patch-wise) reconstructions of equilibrated tractions from local Neumann problems can be found in [2, 10, 25, 32], whereas direct prescription of the degrees of freedom in the Arnold–Winther finite element space is considered in [31].

The second contribution of this work is to perform an a posteriori error analysis of Biot's poro-elasticity problem using the above reconstructed fluxes to compute the error indicators. Equilibrated-flux a posteriori error estimates for poro-elasticity appear to be a novel topic (residual-based error estimates can be found, e.g., in [18,27]). Equilibrated-flux a posteriori error estimates offer several advantages. On the one hand, error upper bounds are obtained with fully computable constants. The idea can be traced back to [34] and was advanced amongst others by [1,9,11,19,21,23,24,26,36]. Another interesting property is the polynomial-degree robustness proved recently for the Poisson problem in [8,21]. A third attractive feature introduced in [20] is to distinguish among various error components, e.g., discretization, linearization, and algebraic solver error components, and to equilibrate adaptively these components in the iterative solution of nonlinear problems. This idea was applied to multi-phase, multi-components (possibly non isothermal) Darcy flows in [14–16]. For simplicity, we consider in the present work a global error measure which lends itself naturally to the development of equilibrated-flux error estimators, and defined as the dual energy-norm of the residual of the weak formulation.

This paper is organized as follows. In Section 2, we introduce the weak and discrete formulations of Biot's poro-elasticity problem (1.1), along with some useful notation and preliminary results. In Section 3, we present the equilibrated reconstruction for the Darcy velocity and the total stress tensor. In Section 4, we derive a fully computable upper bound on the residual dual norm. We then distinguish two different error sources in the upper bound, namely the spatial and the temporal discretization, and we propose an algorithm adapting the mesh and the time step so as to equilibrate these error sources. Finally, we show numerical results in Section 5.

2 Setting

In this section we introduce some notation, the weak formulation, and the discrete solution of problem (1.1).

2.1 Weak formulation

We denote by $L^2(\Omega)$, $\underline{L}^2(\Omega)$ and $\underline{\underline{L}}^2(\Omega)$ the spaces composed of square-integrable functions taking values in $\mathbb{R}$, $\mathbb{R}^2$ and $\mathbb{R}^{2\times 2}$ respectively, and by $(\cdot,\cdot)$ and $\|\cdot\|$ the corresponding inner product and norm. We also let $L^2_0(\Omega) := \{q \in L^2(\Omega) \mid (q,1) = 0\}$. $\underline{H}^1(\Omega)$ stands for the Sobolev space composed of $\underline{L}^2(\Omega)$ functions with weak gradients in $\underline{\underline{L}}^2(\Omega)$ and $\underline{H}^1_0(\Omega)$ for its zero-trace subspace. $\underline{\underline{H}}(\mathrm{div},\Omega)$ and $\underline{H}(\mathrm{div},\Omega)$ denote the spaces composed of $\underline{\underline{L}}^2(\Omega)$ and $\underline{L}^2(\Omega)$ functions

with weak divergence in $\underline{L}^2(\Omega)$ and $L^2(\Omega)$, respectively, $\underline{\underline{H}}_{\rm s}(\mathrm{div},\Omega)$ the subspace of $\underline{\underline{H}}(\mathrm{div},\Omega)$ composed of symmetric-valued tensors, and $\underline{H}_0(\mathrm{div},\Omega) := \{\underline{\varphi} \in \underline{H}(\mathrm{div},\Omega) \mid \underline{\varphi}\cdot\underline{n}_\Omega = 0 \text{ on } \partial\Omega\}$.

We assume henceforth, for the sake of simplicity, that the volumetric body force $\underline{f}$ and the fluid source g lie in $L^2(0,t_F;\underline{L}^2(\Omega))$ and $L^2(0,t_F;L^2_0(\Omega))$, respectively. In order to write a weak formulation of this poro-elastic problem, we define

$$\underline{U} := \underline{H}^1_0(\Omega), \qquad P := H^1(\Omega), \tag{2.1}$$

where in the case $c_0 = 0$ we require additionally that $P = H^1(\Omega)\cap L^2_0(\Omega)$, and introduce the following Bochner spaces:

$$X := L^2(0,t_F;\underline{U}) \times L^2(0,t_F;P), \tag{2.2a}$$
$$Y := H^1(0,t_F;\underline{U}) \times H^1(0,t_F;P). \tag{2.2b}$$

Let $\underline{u},\underline{v}\in\underline{U}$ and $p,q\in P$. We define the bilinear forms

$$a(\underline{u},\underline{v}) := (\underline{\underline{\sigma}}(\underline{u}),\underline{\underline{\epsilon}}(\underline{v})), \tag{2.3a}$$
$$b(\underline{v},q) := -(q,\nabla\cdot\underline{v}), \tag{2.3b}$$
$$c(p,q) := (c_0 p,q), \tag{2.3c}$$
$$d(p,q) := (\kappa\underline{\nabla}p,\underline{\nabla}q). \tag{2.3d}$$

Then, we consider the following weak formulation: find $(\underline{u},p)\in Y$, verifying the initial condition (1.1e) with $\underline{u}_0\in\underline{H}^1_0(\Omega)$ and (1.4) with $p_0\in H^1(\Omega)$ if $c_0>0$, and such that, for a.e. $t\in(0,t_F)$,

$$a(\underline{u}(t),\underline{v}) + b(\underline{v},p(t)) = (\underline{f}(t),\underline{v}) \qquad \forall \underline{v}\in\underline{U}, \tag{2.4a}$$
$$-b(\partial_t\underline{u}(t),q) + c(\partial_t p(t),q) + d(p(t),q) = (g(t),q) \qquad \forall q\in P. \tag{2.4b}$$

The well-posedness of Biot's consolidation problem in slightly different weak formulations is shown in [38, 41]. The uniqueness of the solution to (2.4) can be shown by energy arguments. Assuming the existence of the solution in Y, we denote by $\underline{\underline{\sigma}}(\underline{u})$ the resulting effective stress tensor, by $\underline{\underline{\theta}}(\underline{u},p) = \underline{\underline{\sigma}}(\underline{u}) - p\underline{\underline{I}}_2$ the total stress tensor and by $\underline{\phi}(p) = -\kappa\underline{\nabla}p$ the Darcy velocity. They verify the following properties:

$$\underline{\underline{\theta}}(\underline{u},p)\in L^2(0,t_F;\underline{\underline{H}}_{\rm s}(\mathrm{div},\Omega)), \qquad -\underline{\nabla}\cdot\underline{\underline{\theta}}(\underline{u},p) = \underline{f}, \tag{2.5a}$$
$$\underline{\phi}(p)\in L^2(0,t_F;\underline{H}_0(\mathrm{div},\Omega)), \qquad \nabla\cdot\underline{\phi}(p) = g - \partial_t(\nabla\cdot\underline{u} + c_0 p). \tag{2.5b}$$

2.2 Discrete setting

For the time discretization, we consider a sequence of discrete times $(t^n)_{0\le n\le N}$ such that $t^i < t^j$ whenever $i<j$, $t^0=0$, and $t^N = t_F$. For each $1\le n\le N$, let $I_n := (t^{n-1},t^n)$ and $\tau_n := t^n - t^{n-1}$. For a space-time function v, we denote $v^n := v(\cdot,t^n)$ and define the backward differencing operator $\partial_t^n v = \tau_n^{-1}(v^n - v^{n-1})$.

At each time step $1\le n\le N$, the space discretization is based on a conforming triangulation $\mathcal{T}_h^n$ of Ω, i.e. a set of closed triangles with union equal to $\overline{\Omega}$ and such that, for any distinct $T_1,T_2\in\mathcal{T}_h^n$, the set $T_1\cap T_2$ is either a common edge, a vertex or the empty set. We assume that $\mathcal{T}_h^n$ verifies the minimum angle condition, i.e., there exists $\alpha_{\min}>0$ uniform with respect

to all considered meshes such that the minimum angle α_T of each triangle $T \in \mathcal{T}_h^n$ satisfies $\alpha_T \geq \alpha_{\min}$. The set of vertices of the mesh is denoted by $\mathcal{V}_h^n$; it is decomposed into interior vertices $\mathcal{V}_h^{n,\mathrm{int}}$ and boundary vertices $\mathcal{V}_h^{n,\mathrm{ext}}$. For any subdomain $\omega \subset \Omega$ we denote $\mathcal{V}_\omega^n$ the set of vertices in ω. For all $a \in \mathcal{V}_h^n$, $\mathcal{T}_a^n$ is the patch of elements sharing the vertex a, and ω_a the corresponding open subset of Ω. For all $T \in \mathcal{T}_h^n$, $\mathcal{V}_T^n$ denotes the set of vertices of T, h_T its diameter and $\underline{n}_T$ its unit outward normal vector.

For all $n \in \mathbb{N}$ and all $k \in \mathbb{N}$, we denote by $\mathbb{P}_k(T)$ the space of bivariate polynomials in $T \in \mathcal{T}_h^n$ of total degree at most k and by $\mathbb{P}_k(\mathcal{T}_h^n) = \{\varphi \in L^2(\Omega) \mid \varphi|_T \in \mathbb{P}_k(T)\ \forall T \in \mathcal{T}_h^n\}$ the corresponding broken space over $\mathcal{T}_h^n$.

The following Poincaré's inequality holds for all $T \in \mathcal{T}_h^n$:

$$\|v - \Pi_{0,T} v\|_T \leq C_{P,T} h_T \|\underline{\nabla} v\|_T \qquad \forall v \in H^1(T), \tag{2.6}$$

where $\Pi_{0,T} : L^1(T) \to \mathbb{P}_0(T)$ is such that $\int_T (v - \Pi_{0,T} v) \mathrm{d}\underline{x} = 0$ and $C_{P,T} = 1/\pi$ owing to the convexity of the mesh elements (see e.g. [5]). Let

$$\underline{RM} := \{\underline{b} + c(x_2, -x_1)^{\mathrm{T}} \mid \underline{b} \in \mathbb{R}^2, c \in \mathbb{R}\} \tag{2.7}$$

denote the space of rigid body motions. We have the following Korn's inequality, again valid for all $T \in \mathcal{T}_h^n$:

$$\|\underline{\underline{\nabla}}(\underline{v} - \Pi_{RM,T} \underline{v})\|_T \leq C_{K,T} \|\underline{\underline{\epsilon}}(\underline{v})\|_T \qquad \forall \underline{v} \in \underline{H}^1(T), \tag{2.8}$$

where $\Pi_{RM,T} : \underline{H}^1(T) \to \underline{RM}$ is such that $\int_T (\underline{v} - \Pi_{RM,T} \underline{v}) \mathrm{d}\underline{x} = \underline{0}$ and $\int_T \mathrm{rot}(\underline{v} - \Pi_{RM,T} \underline{v}) \mathrm{d}\underline{x} = 0$ (with $\mathrm{rot}(\underline{v}) := \partial_{x_1} v_2 - \partial_{x_2} v_1$), and the constant $C_{K,T}$ is bounded by $\sqrt{2}(\sin(\alpha_T/4))^{-1}$ (cf [22]). Combining (2.6) and (2.8), and accounting for the bounds on the corresponding constants, we infer that, for all $T \in \mathcal{T}_h^n$,

$$\|\underline{v} - \Pi_{RM,T} \underline{v}\|_T \leq \frac{h_T}{\pi} \frac{\sqrt{2}}{\sin(\alpha_T/4)} \|\underline{\underline{\epsilon}}(\underline{v})\|_T \qquad \forall \underline{v} \in \underline{H}^1(T). \tag{2.9}$$

2.3 Discrete problem

We will focus on the conforming Taylor–Hood finite element method using for each time step $1 \leq n \leq N$ the spaces

$$\underline{U}_h^n := \underline{\mathbb{P}}_{k+1}(\mathcal{T}_h^n) \cap \underline{U}, \quad P_h^n := \mathbb{P}_k(\mathcal{T}_h^n) \cap P, \tag{2.10}$$

with $k \geq 1$. This method was first proposed in [39] for incompressible flows and is known to provide stable pore pressure approximations (cf. [30] and [37, 43]) and is a classical choice for the discretization of poro-mechanical problems by conforming finite elements.

Assumption 2.1 (Piecewise-constant-in-time source terms)**.** *For simplicity of exposition, we assume henceforth that the functions $\underline{f}$ and g are constant-in-time on each time interval I_n and denote $\underline{f}^n := \underline{f}|_{I_n}$ and $g^n := g|_{I_n}$.*

Using the Taylor–Hood finite element spaces and a backward Euler scheme to march in time, the discrete problem reads: given $\underline{u}_h^0$ and, if $c_0 > 0$, p_h^0, find $(\underline{u}_h^n, p_h^n) \in \underline{U}_h^n \times P_h^n$, for all $1 \leq n \leq N$, such that

$$a(\underline{u}_h^n, \underline{v}_h) + b(\underline{v}_h, p_h^n) = (\underline{f}^n, \underline{v}_h) \quad \forall \underline{v}_h \in \underline{U}_h^n, \tag{2.11a}$$

$$-b(\partial_t \underline{u}_{h\tau}^n, q_h) + c(\partial_t p_{h\tau}^n, q_h) + d(p_h^n, q_h) = (g^n, q_h) \quad \forall q_h \in P_h^n, \tag{2.11b}$$

where we denote by $\underline{u}_{h\tau}, p_{h\tau}$ the discrete space-time functions which are continuous and piecewise affine in time, and such that, for each $0 \le n \le N$, $(\underline{u}_{h\tau}, p_{h\tau})(\cdot, t^n) = (\underline{u}_h^n, p_h^n)$, so that $\partial_t \underline{u}_{h\tau}^n := \partial_t \underline{u}_{h\tau}|_{I_n} = \tau_n^{-1}(\underline{u}_h^n - \underline{u}_h^{n-1})$ and $\partial_t p_{h\tau}^n := \partial_t p_{h\tau}|_{I_n} = \tau_n^{-1}(p_h^n - p_h^{n-1})$.

3 Quasi-static flux reconstructions

In contrast to (2.5), we have in general $\underline{\underline{\theta}}(\underline{u}_h^n, p_h^n) \notin \underline{\underline{H}}_{\mathrm{s}}(\mathrm{div}, \Omega)$ and $\underline{\phi}(p_h^n) \notin \underline{H}_0(\mathrm{div}, \Omega)$. In this section, we restore these properties by reconstructing $H(\mathrm{div})$-conforming discrete fluxes. These reconstructions are devised locally on patches of elements around mesh vertices. We first present the reconstructions in an abstract setting; then we apply these reconstructions to Biot's poro-elasticity problem. Since the time variable is irrelevant in devising the reconstructions, we drop the index n in the abstract presentation.

3.1 Darcy velocity

We reconstruct the Darcy velocity using mixed Raviart–Thomas finite elements of order $l \ge 0$. For each element $T \in \mathcal{T}_h$, the local Raviart–Thomas polynomial spaces are defined by

$$\underline{W}_T := \underline{\mathbb{P}}_l(T) + \underline{x}\mathbb{P}_l(T), \tag{3.1a}$$

$$Q_T = \mathbb{P}_l(T). \tag{3.1b}$$

Figure 1 shows the corresponding degrees of freedom for $l = 0$ and $l = 1$. For each vertex $a \in \mathcal{V}_h$, the mixed Raviart–Thomas finite element spaces on the patch domain ω_a are then defined as

$$\tilde{\underline{W}}_h^a := \{\underline{v}_h \in \underline{H}(\mathrm{div}, \omega_a) \mid \underline{v}_h|_T \in \underline{W}_T \ \forall T \in \mathcal{T}_a\}, \tag{3.2a}$$

$$\tilde{Q}_h^a := \{q_h \in L^2(\omega_a) \mid q_h|_T \in Q_T \ \forall T \in \mathcal{T}_a\}. \tag{3.2b}$$

We need to consider the following subspaces associated with the setting where a zero normal component is enforced on the velocity:

$$\underline{W}_h^a := \{\underline{v}_h \in \tilde{\underline{W}}_h^a \mid \underline{v}_h \cdot \underline{n}_{\omega_a} = 0 \text{ on } \partial\omega_a\}, \tag{3.3a}$$

$$Q_h^a := \{q_h \in \tilde{Q}_h^a \mid (q_h, 1)_{\omega_a} = 0\}. \tag{3.3b}$$

The distribution of the degrees of freedom of functions in $\underline{W}_h^a$ is presented in Figure 2. Note that we enforce the zero normal condition also on patches associated with boundary vertices since a zero normal Darcy velocity is prescribed in the exact problem; see Remark 3.3 for other types of boundary conditions.

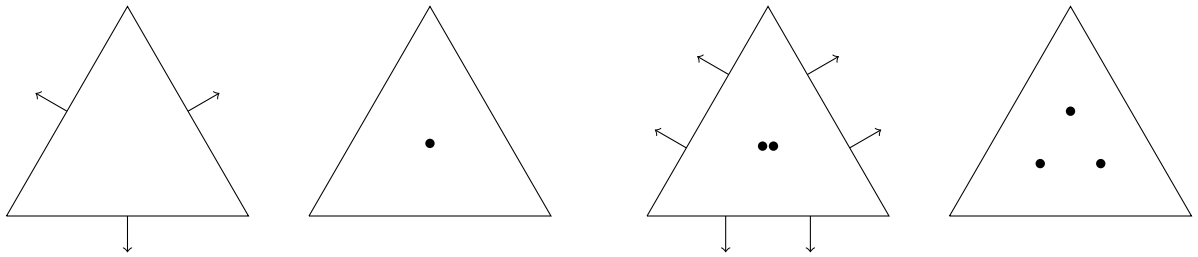

Figure 1: The mixed Raviart–Thomas finite element for $l = 0$ (left) and $l = 1$ (right)

Construction 3.1 (Darcy velocity $\underline{\phi}_h$)**.** *For each $a \in \mathcal{V}_h$, let $\gamma_a \in L^2(\omega_a)$ be such that $(\gamma_a, 1)_{\omega_a} = 0$, and let $\underline{\Gamma}_a \in \underline{L}^2(\omega_a)$. Consider the following constrained minimization problem:*

$$\underline{\varphi}_h^a = \underset{\underline{w}_h \in \underline{W}_h^a,\ \nabla\cdot\underline{w}_h = \Pi_{Q_h^a}\gamma_a}{\operatorname{argmin}} \|\underline{w}_h - \underline{\Gamma}_a\|_{\omega_a}, \tag{3.4}$$

where $\Pi_{Q_h^a}$ denotes the L^2–orthogonal projection on Q_h^a. Then, extending $\underline{\varphi}_h^a$ by zero outside ω_a, set

$$\underline{\phi}_h := \sum_{a\in\mathcal{V}_h} \underline{\varphi}_h^a. \tag{3.5}$$

Since functions in $\underline{W}_h^a$ have zero normal component on $\partial\omega_a$, condition $(\gamma_a, 1)_{\omega_a} = 0$ is crucial for the well-posedness of the constrained minimization problem (3.4). This problem is classically solved by finding $\underline{\varphi}_h^a \in \underline{W}_h^a$ and $s_h^a \in Q_h^a$ such that

$$\left(\underline{\varphi}_h^a, \underline{w}_h\right)_{\omega_a} - (s_h^a, \nabla\cdot\underline{w}_h)_{\omega_a} = (\underline{\Gamma}_a, \underline{w}_h)_{\omega_a} \quad \forall \underline{w}_h \in \underline{W}_h^a, \tag{3.6a}$$

$$\left(\nabla\cdot\underline{\varphi}_h^a, q_h\right)_{\omega_a} = (\gamma_a, q_h)_{\omega_a} \quad \forall q_h \in Q_h^a. \tag{3.6b}$$

This problem is well-posed owing to the properties of mixed Raviart–Thomas finite elements, and we obtain the following result (cf. [9, 11, 21]):

Lemma 3.2 (Properties of $\underline{\phi}_h$)**.** *Let $\underline{\phi}_h$ be prescribed by Construction 3.1. Then, $\underline{\phi}_h \in \underline{H}_0(\mathrm{div}, \Omega)$, and letting $\gamma_h \in L^2(\Omega)$ be defined such that $\gamma_h|_T = \sum_{a\in\mathcal{V}_T} \gamma_a$ for all $T \in \mathcal{T}_h$, we have*

$$(\gamma_h - \nabla\cdot\underline{\phi}_h, q)_T = 0 \qquad \forall q \in Q_T \quad \forall T \in \mathcal{T}_h. \tag{3.7}$$

Remark 3.3 (Other boundary conditions)**.** *Suppose that we are given a partition of the boundary as $\partial\Omega = \partial\Omega_{N,P} \cup \partial\Omega_{D,P}$ (the subsets $\partial\Omega_{N,P}$ and $\partial\Omega_{D,P}$ are conventionally closed in $\partial\Omega$, i.e., $\partial\Omega_{N,P} \cap \partial\Omega_{D,P}$ is the common boundary of the two subsets) and that an inhomogeneous Neumann condition is enforced on the flux $\phi(p)$ on $\partial\Omega_{N,P}$ (and a Dirichlet condition is enforced on p in $\partial\Omega_{D,P}$). Assume that the mesh is fitted to the boundary partition, so that any mesh edge on the boundary belongs to either $\partial\Omega_{N,P}$ or $\partial\Omega_{D,P}$. As detailed in [17], this situation can be accommodated in Construction 3.1 up to minor modifications for all $a \in \mathcal{V}_h^{\mathrm{ext}}$ (the construction is unmodified for all $a \in \mathcal{V}_h^{\mathrm{int}}$). For the flux, we consider for the trial and test spaces, respectively,*

$$\underline{W}_{h,N}^a := \{\underline{w}_h \in \underline{\tilde{W}}_h^a \mid \underline{w}_h\cdot\underline{n}_{\omega_a}|_{\partial\omega_a\setminus\partial\Omega} = 0,\ \underline{w}_h\cdot\underline{n}_{\omega_a}|_{\partial\omega_a\cap\partial\Omega_{N,P}} = \Phi_{a,N}\},$$
$$\underline{W}_{h,0}^a := \{\underline{w}_h \in \underline{\tilde{W}}_h^a \mid \underline{w}_h\cdot\underline{n}_{\omega_a}|_{\partial\omega_a\setminus\partial\Omega} = 0,\ \underline{w}_h\cdot\underline{n}_{\omega_a}|_{\partial\omega_a\cap\partial\Omega_{N,P}} = 0\},$$

with $\Phi_{a,N}$ related to the Neumann condition, whereas we set $Q_h^a := \tilde{Q}_h^a$ if a lies on some edge in $\partial\Omega_{D,P}$ and Q_h^a as in (3.3b) *otherwise.*

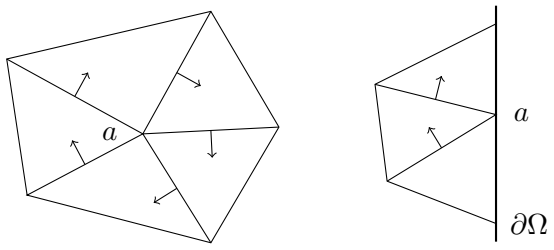

Figure 2: The degrees of freedom of the space $\underline{W}_h^a$ in the case $l = 0$ on a patch for $a \in \mathcal{V}_h^{\mathrm{int}}$ (left) and $a \in \mathcal{V}_h^{\mathrm{ext}}$ (right)

3.2 Total stress tensor

We reconstruct the total stress tensor using mixed Arnold–Winther finite elements of order $m \geq 1$. One advantage of using these elements is that the reconstructed stress tensor is symmetric. For each element $T \in \mathcal{T}_h$, the local Arnold–Winther polynomial spaces are defined by

$$\begin{aligned} \underline{\underline{\Sigma}}_T &:= \underline{\underline{\mathbb{P}}}_{s,m+1}(T) + \{\underline{\underline{\tau}} \in \underline{\underline{\mathbb{P}}}_{s,m+2}(T) \mid \underline{\nabla} \cdot \underline{\underline{\tau}} = \underline{0}\} && \text{(3.8a)} \\ &= \{\underline{\underline{\tau}} \in \underline{\underline{\mathbb{P}}}_{s,m+2}(T) \mid \underline{\nabla} \cdot \underline{\underline{\tau}} \in \underline{\mathbb{P}}_m(T)\}, \\ \underline{V}_T &:= \underline{\mathbb{P}}_m(T), && \text{(3.8b)} \end{aligned}$$

where $\underline{\underline{\mathbb{P}}}_{s,m}(T)$ denotes the subspace of $\underline{\underline{\mathbb{P}}}_m(T)$ composed of symmetric-valued tensors. Figure 3 shows the corresponding degrees of freedom in the cases $m = 1$ and $m = 2$. The dimension of $\underline{V}_T$ is $(m+1)(m+2)$, and it is shown in [4] that $\dim(\underline{\underline{\Sigma}}_T) = (3m^2 + 17m + 28)/2$. For the lowest-order case $m = 1$, the 24 degrees of freedom in $\underline{\underline{\Sigma}}_T$ are

- The values of the three components of the (symmetric) stress tensor at each vertex of the triangle (9 dofs);
- The values of the moments of degree 0 and 1 of the normal components of the stress tensor on each edge (12 dofs);
- The value of the moment of degree 0 of each component of the stress tensor on the triangle (3 dofs).

For each vertex $a \in \mathcal{V}_h$, the mixed Arnold–Winther finite element spaces on the patch domain ω_a are defined as

$$\begin{aligned} \tilde{\underline{\underline{\Sigma}}}_h^a &:= \{\underline{\underline{\tau}}_h \in \underline{\underline{H}}_{\mathrm{s}}(\mathrm{div}, \omega_a) \mid \underline{\underline{\tau}}_h|_T \in \underline{\underline{\Sigma}}_T \ \forall T \in \mathcal{T}_a\}, && \text{(3.9a)} \\ \tilde{\underline{V}}_h^a &:= \{\underline{v}_h \in \underline{L}^2(\omega_a) \mid \underline{v}_h|_T \in \underline{V}_T \ \forall T \in \mathcal{T}_a\}. && \text{(3.9b)} \end{aligned}$$

We need to consider subspaces where a zero normal component is enforced on the stress tensor. Since the boundary condition in the exact problem prescribes the displacement and not the normal stress, we distinguish the case whether a is an interior vertex or a boundary vertex (see Remark 3.6 for other types of boundary conditions). For $a \in \mathcal{V}_h^{\mathrm{int}}$, we set

$$\begin{aligned} \underline{\underline{\Sigma}}_h^a &:= \{\underline{\underline{\tau}}_h \in \tilde{\underline{\underline{\Sigma}}}_h^a \mid \underline{\underline{\tau}}_h \underline{n}_{\omega_a} = \underline{0} \text{ on } \partial\omega_a, \ \underline{\underline{\tau}}_h(b) = \underline{\underline{0}} \ \forall b \in \mathcal{V}_{\omega_a} \cap \partial\omega_a\}, && \text{(3.10a)} \\ \underline{V}_h^a &:= \{\underline{v}_h \in \tilde{\underline{V}}_h^a \mid (\underline{v}_h, \underline{z})_{\omega_a} = 0 \ \forall \underline{z} \in \underline{RM}\}, && \text{(3.10b)} \end{aligned}$$

and for $a \in \mathcal{V}_h^{\mathrm{ext}}$, we set

$$\begin{aligned} \underline{\underline{\Sigma}}_h^a &:= \{\underline{\underline{\tau}}_h \in \tilde{\underline{\underline{\Sigma}}}_h^a \mid \underline{\underline{\tau}}_h \underline{n}_{\omega_a} = \underline{0} \text{ on } \partial\omega_a \backslash \partial\Omega, \ \underline{\underline{\tau}}_h(b) = \underline{\underline{0}} \ \forall b \in \mathcal{V}_{\omega_a} \cap (\partial\omega_a \backslash \partial\Omega)\}, && \text{(3.11a)} \\ \underline{V}_h^a &:= \tilde{\underline{V}}_h^a. && \text{(3.11b)} \end{aligned}$$

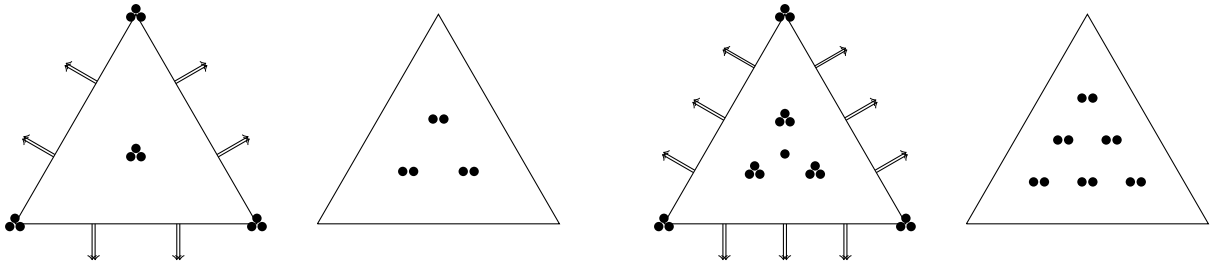

Figure 3: Element diagrams for the pair $(\underline{\underline{\Sigma}}_T, \underline{V}_T)$ in the cases $m = 1$ (left) and $m = 2$ (right)

Note that, as argued in [4], the nodal degrees of freedom on $\partial\omega_a$ are set to zero if the vertex separates two edges where the normal stress is enforced to be zero. The distribution of the degrees of freedom in $\underline{\underline{\Sigma}}_h^a$ is presented in Figure 4.

Construction 3.4 (Total stress tensor $\underline{\underline{\theta}}_h$)**.** *For each $a \in \mathcal{V}_h$, let $\underline{\lambda}_a \in \underline{L}^2(\omega_a)$ be such that $(\underline{\lambda}_a, \underline{z})_{\omega_a} = 0$ for all $\underline{z} \in \underline{RM}$ and all $a \in \mathcal{V}_h^{\rm int}$, and let $\underline{\underline{\Lambda}}_a \in \underline{\underline{L}}^2(\omega_a)$. Consider the following constrained minimization problem:*

$$\underline{\underline{\vartheta}}_h^a = \operatorname*{argmin}_{\underline{\underline{\tau}}_h \in \underline{\underline{\Sigma}}_h^a,\ \underline{\nabla}\cdot\underline{\underline{\tau}}_h = \Pi_{\underline{V}_h^a}\underline{\lambda}_a} \|\underline{\underline{\tau}}_h - \underline{\underline{\Lambda}}_a\|_{\omega_a}, \tag{3.12}$$

where $\Pi_{\underline{V}_h^a}$ denotes the L^2-orthogonal projection onto $\underline{V}_h^a$. Then, extending $\underline{\underline{\vartheta}}_h^a$ by zero outside ω_a, set

$$\underline{\underline{\theta}}_h := \sum_{a\in\mathcal{V}_h} \underline{\underline{\vartheta}}_h^a. \tag{3.13}$$

The condition on $\underline{\lambda}_a$ for all $a \in \mathcal{V}_h^{\rm int}$ ensures that the constrained minimization problem (3.12) is well-posed. This problem is classically solved by finding $\underline{\underline{\vartheta}}_h^a \in \underline{\underline{\Sigma}}_h^a$ and $\underline{s}_h^a \in \underline{V}_h^a$ such that

$$\left(\underline{\underline{\vartheta}}_h^a, \underline{\underline{\tau}}_h\right)_{\omega_a} - \left(\underline{s}_h^a, \underline{\nabla}\cdot\underline{\underline{\tau}}_h\right)_{\omega_a} = \left(\underline{\underline{\Lambda}}_a, \underline{\underline{\tau}}_h\right)_{\omega_a} \qquad \forall \underline{\underline{\tau}}_h \in \underline{\underline{\Sigma}}_h^a, \tag{3.14a}$$

$$\left(\underline{\nabla}\cdot\underline{\underline{\vartheta}}_h^a, \underline{v}_h\right)_{\omega_a} = (\underline{\lambda}_a, \underline{v}_h)_{\omega_a} \qquad \forall \underline{v}_h \in \underline{V}_h^a. \tag{3.14b}$$

This problem is well-posed (see [4]), and we obtain the following result:

Lemma 3.5 (Properties of $\underline{\underline{\theta}}_h$)**.** *Let $\underline{\underline{\theta}}_h$ be prescribed by Construction 3.4. Then, $\underline{\underline{\theta}}_h \in \underline{\underline{H}}_{\rm s}(\mathrm{div}, \Omega)$, and letting $\underline{\lambda}_h \in \underline{L}^2(\Omega)$ be defined such that $\underline{\lambda}_h|_T = \sum_{a\in\mathcal{V}_T} \underline{\lambda}_a$ for all $T \in \mathcal{T}_h$, we have*

$$(\underline{\lambda}_h - \underline{\nabla}\cdot\underline{\underline{\theta}}_h, \underline{v})_T = 0 \qquad \forall \underline{v} \in \underline{V}_T \quad \forall T \in \mathcal{T}_h. \tag{3.15}$$

Proof. All the fields $\underline{\underline{\vartheta}}_h^a$ are in $\underline{\underline{H}}_{\rm s}(\mathrm{div}, \omega_a)$ and satisfy appropriate zero normal conditions so that their zero-extension to Ω is in $\underline{\underline{H}}_{\rm s}(\mathrm{div}, \Omega)$. Hence, $\underline{\underline{\theta}}_h \in \underline{\underline{H}}_{\rm s}(\mathrm{div}, \Omega)$. Let us prove (3.15). Let $a \in \mathcal{V}_h^{\rm int}$. Since $(\underline{\lambda}_a, \underline{z})_{\omega_a} = 0$ for all $\underline{z} \in \underline{RM}$, we infer that (3.14b) actually holds for all $\underline{v}_h \in \tilde{\underline{V}}_h^a$. The same holds true if $a \in \mathcal{V}_h^{\rm ext}$ by definition of $\underline{V}_h^a$. Hence, $\left(\underline{\nabla}\cdot\underline{\underline{\vartheta}}_h^a, \underline{v}_h\right)_{\omega_a} = (\underline{\lambda}_a, \underline{v}_h)_{\omega_a}$ for all $\underline{v}_h \in \tilde{\underline{V}}_h^a$ and all $a \in \mathcal{V}_h$. Since $\tilde{\underline{V}}_h^a$ is composed of piecewise polynomials that can be chosen independently in each cell $T \in \mathcal{T}_a$, we conclude that (3.15) holds. □

Remark 3.6 (Other boundary conditions)**.** *In the spirit of Remark 3.3 with the boundary partition $\partial\Omega = \partial\Omega_{N,U} \cup \partial\Omega_{D,U}$, the minor modifications of Construction 3.4 are as follows for*

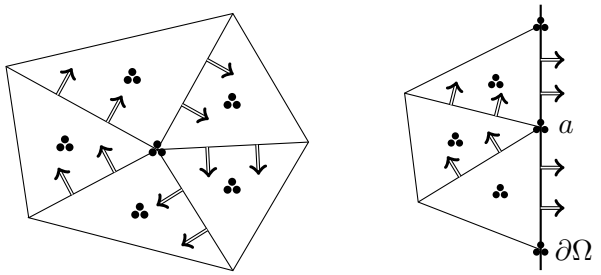

Figure 4: The degrees of freedom of the space $\underline{\underline{\Sigma}}_h^a$ in the case $m = 1$ on a patch for $a \in \mathcal{V}_h^{\rm int}$ (left) and $a \in \mathcal{V}_h^{\rm ext}$ (right)

all $a \in \mathcal{V}_h^{\rm ext}$ (the construction is unmodified for all $a \in \mathcal{V}_h^{\rm int}$): For the stress tensor, we consider for the trial and test spaces, respectively,

$$\begin{aligned}
\underline{\underline{\Sigma}}_{h,N}^a &:= \{\underline{\underline{\tau}}_h \in \underline{\underline{\tilde{\Sigma}}}_h^a \mid \underline{\underline{\tau}}_h\underline{n}_{\omega_a}|_{\partial\omega_a\setminus\partial\Omega} = \underline{0},\ \underline{\underline{\tau}}_h\underline{n}_{\omega_a}|_{\partial\omega_a\cap\partial\Omega_{N,U}} = \underline{\Theta}_{a,N},\\
&\qquad \underline{\underline{\tau}}_h(b) = \underline{\underline{0}}\ \forall b \in \mathcal{V}_{\omega_a} \cap (\partial\omega_a\setminus\partial\Omega),\ \underline{\underline{\tau}}_h(b) = \underline{\underline{\theta}}_{a,N}\ \forall b \in \mathcal{V}_{\omega_a} \cap (\partial\Omega \setminus \partial\Omega_{D,U})\},\\
\underline{\underline{\Sigma}}_{h,0}^a &:= \{\underline{\underline{\tau}}_h \in \underline{\underline{\tilde{\Sigma}}}_h^a \mid \underline{\underline{\tau}}_h\underline{n}_{\omega_a}|_{\partial\omega_a\setminus\partial\Omega} = \underline{0},\ \underline{\underline{\tau}}_h\underline{n}_{\omega_a}|_{\partial\omega_a\cap\partial\Omega_{N,U}} = \underline{0},\\
&\qquad \underline{\underline{\tau}}_h(b) = \underline{\underline{0}}\ \forall b \in \mathcal{V}_{\omega_a} \cap (\partial\omega_a\setminus\partial\Omega),\ \underline{\underline{\tau}}_h(b) = \underline{\underline{0}}\ \forall b \in \mathcal{V}_{\omega_a} \cap (\partial\Omega \setminus \partial\Omega_{D,U})\},
\end{aligned}$$

with $\underline{\Theta}_{a,N}$ and $\underline{\underline{\theta}}_{a,N}$ related to the Neumann condition, whereas we set $\underline{V}_h^a$ as in (3.11b) *if a lies on some edge in $\partial\Omega_{D,U}$ and $\underline{V}_h^a$ as in* (3.10b) *otherwise.*

Remark 3.7 (Extension to 3D)**.** *The extension of Construction 3.4 to three dimensions hinges on the existence of mixed finite element spaces producing three dimensional, $\underline{\underline{H}}(\mathrm{div})$-conforming, symmetric tensors. These were introduced in [3], but are complex to implement and require significant computational effort, due to the high number of degrees of freedom per element (162 for the stress tensor).*

3.3 Application to Biot's poro-elasticity problem

In this section, we apply the above constructions to the discrete Biot poro-elasticity problem (2.11). The reconstructed Darcy velocity and total stress tensor are space-time functions that are piecewise constant in time, i.e. these functions are calculated at every time step. We use Constructions 3.1 and 3.4 where we now specify the data γ_a, $\underline{\Gamma}_a$, $\underline{\lambda}_a$, and $\underline{\underline{\Lambda}}_a$ for each $1 \le n \le N$. For this purpose, we consider for any mesh vertex $a \in \mathcal{V}_h^n$, the piecewise affine "hat" function $\psi_a \in \mathbb{P}_1(\mathcal{T}_h) \cap H^1(\Omega)$ supported in ω_a, which takes the value 1 at the vertex a and zero at the vertices lying on the boundary of ω_a; cf. Figure 5. An important property for our constructions is the following partition of unity:

$$\sum_{a\in\mathcal{V}_T^n} \psi_a|_T = 1 \qquad \forall T \in \mathcal{T}_h^n. \tag{3.16}$$

Construction 3.8 (Darcy velocity and total stress reconstructions)**.** *Let $1 \le n \le N$. Define for all $a \in \mathcal{V}_h^n$,*

$$\gamma_a = \psi_a g^n - \psi_a \partial_t(\nabla\cdot\underline{u}_{h\tau} + c_0 p_{h\tau})^n + \underline{\nabla}\psi_a \cdot \underline{\phi}(p_h^n), \qquad \underline{\Gamma}_a = \psi_a \underline{\phi}(p_h^n), \tag{3.17a}$$

$$\underline{\lambda}_a = -\psi_a \underline{f}^n + \underline{\underline{\theta}}(\underline{u}_h^n, p_h^n)\underline{\nabla}\psi_a, \qquad \underline{\underline{\Lambda}}_a = \psi_a \underline{\underline{\theta}}(\underline{u}_h^n, p_h^n), \tag{3.17b}$$

where we recall that $\underline{\phi}(p_h^n) = -\kappa\nabla p_h^n$ and $\underline{\underline{\theta}}(\underline{u}_h^n, p_h^n) = \underline{\underline{\sigma}}(\underline{u}_h^n) - p_h^n\underline{\underline{I}}_2$. Then define $\underline{\phi}_h^n \in \underline{H}_0(\mathrm{div},\Omega)$ and $\underline{\underline{\theta}}_h^n \in \underline{\underline{H}}_{\rm s}(\mathrm{div},\Omega)$ using Constructions 3.1 and 3.4, respectively, with $l \in \{k-1, k\}$ and $m = k$, where k is the degree of the used Taylor–Hood element in (2.11)*.*

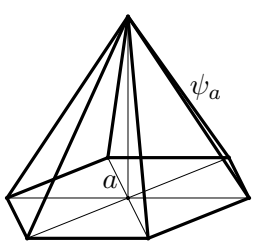

Figure 5: Hat function

Remark 3.9 (Choice of l and m in Construction 3.8)**.** *The polynomial degree k in the Taylor–Hood finite element method* (2.10) *corresponds to degree k for the pressure and degree $k+1$ for the displacement, implying polynomial degree $k-1$ for $\underline{\phi}(p_h)$ and k for $\underline{\underline{\theta}}(\underline{u}_h, p_h)$. Thus, it seems reasonable that the polynomial degree for the reconstruction of the velocity is one lower than for the reconstruction of the total stress tensor. It has been shown in [8, 21] that $k-1$ or k are suitable choices for the velocity reconstruction, and for $k=1$ we can observe the expected convergence rates for $l=0$ and $m=1$ in the numerical test of Section 5.2.*

Lemma 3.10 (Darcy velocity and total stress reconstructions)**.** *Construction 3.8 is well defined, and the following holds:*

$$(-\underline{\nabla}\cdot\underline{\underline{\theta}}_h^n, \underline{z})_T = (\underline{f}^n, \underline{z})_T \qquad \forall T\in\mathcal{T}_h^n,\quad \forall \underline{z}\in\underline{RM}, \tag{3.18a}$$

$$(\nabla\cdot\underline{\phi}_h^n, 1)_T = (g^n - \partial_t(\nabla\cdot\underline{u}_{h\tau} + c_0 p_{h\tau})^n, 1)_T \qquad \forall T\in\mathcal{T}_h^n. \tag{3.18b}$$

Proof. Construction 3.1 is well defined provided $(\gamma_a, 1)_{\omega_a} = 0$ holds for all $a\in\mathcal{V}_h$, and this follows by taking $q_h = \psi_a$ in (2.11b) (this is possible since hat functions are contained in the discrete space for the pressure). Construction 3.4 is well defined provided $(\lambda_a, \underline{z})_{\omega_a} = 0$ for all $\underline{z}\in\underline{RM}$ and all $a\in\mathcal{V}_h^{n,\mathrm{int}}$, and this follows by taking $\underline{v}_h = \psi_a\underline{z}$ in (2.11a) (recall that $k\geq 1$ in (2.10), so that this choice is legitimate) and using that

$$\begin{aligned}(\underline{\underline{\theta}}(\underline{u}_h^n, p_h^n), \underline{\epsilon}(\psi_a\underline{z})) &= (\underline{\underline{\theta}}(\underline{u}_h^n, p_h^n), \underline{\nabla}(\psi_a\underline{z})^{\mathrm{T}})\\ &= (\underline{\underline{\theta}}(\underline{u}_h^n, p_h^n), \underline{z}(\underline{\nabla}\psi_a)^{\mathrm{T}}) + (\underline{\underline{\theta}}(\underline{u}_h^n, p_h^n), \psi_a(\underline{\nabla}\underline{z})^{\mathrm{T}})\\ &= (\underline{\underline{\theta}}(\underline{u}_h^n, p_h^n), \underline{z}(\underline{\nabla}\psi_a)^{\mathrm{T}}).\end{aligned}$$

Finally, the properties on the divergence follow from Lemmas 3.5 and 3.2 and the partition of unity (3.16) which implies that $\sum_{a\in\mathcal{V}_T^n}\nabla\psi_a|_T = \underline{0}$. □

Remark 3.11 (Other boundary conditions)**.** *If inhomogeneous Neumann boundary conditions $\underline{\phi}(p)\cdot\underline{n}_\Omega = \Phi_N$ or $\underline{\underline{\theta}}(\underline{u}, p)\underline{n}_\Omega = \underline{\Theta}_N$ are imposed on $\partial\Omega_{N,P}$ and $\partial\Omega_{N,U}$, respectively, we modify the constructions using Remarks 3.3 and 3.6. In particular, in Remark 3.3, $\Phi_{a,N}$ is the L^2-projection of $\psi_a\Phi_N$ onto $\underline{\tilde{W}}_h^a\cdot\underline{n}_\Omega$, whereas in Remark 3.6, $\underline{\Theta}_{a,N}$ is the L^2-projection of $\psi_a\underline{\Theta}_N$ onto $\underline{\underline{\tilde{\Sigma}}}_h^a\underline{n}_\Omega$.*

4 A posteriori error analysis and space-time adaptivity

In this section, we derive an a posteriori error estimate at every time step n based on the quasi-equilibrated flux reconstructions of Section 3.3 for Biot's poro-elasticity problem. Using these estimators, we devise an adaptive algorithm including the adaptive choice of the mesh size and of the time step.

4.1 A posteriori error estimate

To derive the a posteriori error estimate, we consider the residual of the weak formulation (2.4). To combine the two equations in (2.4) into a single residual, the two equations must be written using the same physical units. Therefore, we introduce a reference time scale $t^\star$ and a reference length scale $l^\star$ which we will use as scaling parameters together with the Young

modulus $E = \mu(3\lambda + 2\mu)(\lambda + \mu)^{-1}$. Defining the bilinear map $\mathcal{B} : Y \times X \to L^2(0, t_F; \mathbb{R})$ such that

$$\mathcal{B}((\underline{u}, p), (\underline{v}, q))(t) := a(\underline{u}, \underline{v})(t) + b(\underline{v}, p)(t) + t^\star \left(-b(\partial_t \underline{u}, q)(t) + c(\partial_t p, q)(t) + d(p, q)(t)\right), \quad (4.1)$$

we can restate (2.4) as follows: find $(\underline{u}, p) \in Y$, verifying the initial condition (1.1e), and (1.4) if $c_0 > 0$, and such that for a.e. $t \in (0, t_F)$,

$$\mathcal{B}((\underline{u}, p), (\underline{v}, q))(t) = (\underline{f}, \underline{v})(t) + t^\star (g, q)(t) \qquad \forall (\underline{v}, q) \in X. \quad (4.2)$$

For any pair $(\underline{u}_{h\tau}, p_{h\tau}) \in Y$, we define the residual $\mathcal{R}(\underline{u}_{h\tau}, p_{h\tau}) \in X'$ of (4.2) as

$$\langle \mathcal{R}(\underline{u}_{h\tau}, p_{h\tau}), (\underline{v}, q) \rangle_{X',X} := \int_0^{t_F} \mathcal{B}((\underline{u} - \underline{u}_{h\tau}, p - p_{h\tau}), (\underline{v}, q))(t) \mathrm{d}t.$$

Its dual norm is defined as

$$\|\mathcal{R}(\underline{u}_{h\tau}, p_{h\tau})\|_{X'} := \sup_{(\underline{v},q) \in X, \|(\underline{v},q)\|_X = 1} \langle \mathcal{R}(\underline{u}_{h\tau}, p_{h\tau}), (\underline{v}, q) \rangle_{X',X},$$

with

$$\|(\underline{v}, q)\|_X^2 := \int_0^{t_F} (E\|\underline{\underline{\epsilon}}(\underline{v})\|)^2 + (l^\star \|\underline{\nabla} q\|)^2 \mathrm{d}t.$$

We first derive a local-in-time a posteriori error estimate. Let the time step $1 \le n \le N$ be fixed. Let us set

$$X_n := L^2(I_n; \underline{U}) \times L^2(I_n; P) \quad \text{and} \quad Y_n := H^1(I_n; \underline{U}) \times H^1(I_n; P),$$

and define the norm $\|\cdot\|_{X_n}$ on X_n in the same way as $\|\cdot\|_X$ on X. The local error measure for the time step n is then defined as

$$\begin{aligned} e^n &:= \sup_{(\underline{v},q) \in X_n, \|(\underline{v},q)\|_{X_n} = 1} \int_{I_n} \mathcal{B}((\underline{u} - \underline{u}_{h\tau}, p - p_{h\tau}), (\underline{v}, q)) \mathrm{d}t \\ &= \sup_{(\underline{v},q) \in X_n, \|(\underline{v},q)\|_{X_n} = 1} \int_{I_n} e_U^n(\underline{v}) + e_P^n(q) \mathrm{d}t, \end{aligned} \quad (4.3)$$

with

$$e_U^n(\underline{v}) := \int_{I_n} (\underline{\underline{\theta}}(\underline{u}, p) - \underline{\underline{\theta}}(\underline{u}_{h\tau}, p_{h\tau}), \underline{\underline{\epsilon}}(\underline{v}))(t) \mathrm{d}t, \quad (4.4a)$$

$$e_P^n(q) := t^\star \int_{I_n} \big(\partial_t(\nabla \cdot \underline{u} + c_0 p) - \partial_t(\nabla \cdot \underline{u}_{h\tau} + c_0 p_{h\tau}), q\big)^n(t) - \big(\underline{\phi}(p) - \underline{\phi}(p_{h\tau}), \underline{\nabla} q\big)(t) \mathrm{d}t, \quad (4.4b)$$

where we recall that $I_n = (t^{n-1}, t^n)$ and that both $\underline{u}_{h\tau}$ and $p_{h\tau}$ are continuous, piecewise affine functions in time.

For all $1 \le n \le N$, let $\underline{\phi}_h^n$ and $\underline{\underline{\theta}}_h^n$ be the constant in time fields over I_n defined by Construction 3.8. For all $T \in \mathcal{T}_h^n$, we define the *residual estimators* $\eta_{R,T,U}^n$, $\eta_{R,T,P}^n$ by

$$\eta_{R,T,U}^n := \frac{h_T}{\pi} \frac{\sqrt{2}}{\sin(\alpha_T/4)} E^{-1} \|\underline{f}^n + \underline{\nabla} \cdot \underline{\underline{\theta}}_h^n\|_T, \quad (4.5a)$$

$$\eta_{R,T,P}^n := \frac{h_T}{\pi} \frac{t^\star}{l^\star} \|g^n - \partial_t^n(\nabla \cdot \underline{u}_{h\tau} + c_0 p_{h\tau}) - \nabla \cdot \underline{\phi}_h^n\|_T, \quad (4.5b)$$

where α_T denotes the minimum angle of the triangle T, and the *flux estimators* $\eta^n_{F,T,U}(t)$, $\eta^n_{F,T,P}(t)$, $t \in I_n$, by

$$\eta^n_{F,T,U}(t) := E^{-1}\|\underline{\underline{\theta}}^n_h - \underline{\underline{\theta}}(\underline{u}_{h\tau}, p_{h\tau})(t)\|_T, \tag{4.6a}$$

$$\eta^n_{F,T,P}(t) := \frac{t^\star}{l^\star}\|\underline{\phi}^n_h - \underline{\phi}(p_{h\tau})(t)\|_T. \tag{4.6b}$$

Theorem 4.1 (Local-in-time a posteriori error estimate)**.** *Let $(\underline{u}, p) \in Y$ be the weak solution of* (2.4) *and let $(\underline{u}_{h\tau}, p_{h\tau}) \in Y$ be the discrete solution of* (2.11)*. Let $1 \le n \le N$. Let e^n be defined by* (4.3) *with estimators defined by* (4.5) *and* (4.6)*. Then the following holds:*

$$e^n \le \left(\int_{I_n} \sum_{T\in\mathcal{T}^n_h} \{(\eta^n_{R,T,U} + \eta^n_{F,T,U}(t))^2 + (\eta^n_{R,T,P} + \eta^n_{F,T,P}(t))^2\}\mathrm{d}t\right)^{1/2}. \tag{4.7}$$

Proof. Let $(\underline{v}, q) \in X_n$. Recalling (4.4a), we have

$$\begin{aligned} e^n_U(\underline{v}) &= \int_{I_n} \big(\underline{\underline{\theta}}(\underline{u}, p) - \underline{\underline{\theta}}(\underline{u}_{h\tau}, p_{h\tau}), \underline{\underline{\epsilon}}(\underline{v})\big)(t)\mathrm{d}t \\ &= \int_{I_n} \big(\underline{f}, \underline{v}\big)(t) - \big(\underline{\underline{\theta}}(\underline{u}_{h\tau}, p_{h\tau}), \underline{\underline{\epsilon}}(\underline{v})\big)(t)\mathrm{d}t \\ &= \int_{I_n} \Big(\underbrace{\big(\underline{f}^n + \underline{\nabla}\cdot\underline{\underline{\theta}}^n_h, \underline{v}(t)\big)}_{\mathfrak{T}_1(t)} + \underbrace{\big(\underline{\underline{\theta}}^n_h - \underline{\underline{\theta}}(\underline{u}_{h\tau}, p_{h\tau}), \underline{\underline{\epsilon}}(\underline{v})\big)(t)}_{\mathfrak{T}_2(t)}\Big)\mathrm{d}t, \end{aligned} \tag{4.8}$$

where we have used (2.4a) to pass to the second line and we have inserted $(\underline{\nabla}\cdot\underline{\underline{\theta}}^n_{h\tau}, \underline{v}) + (\underline{\underline{\theta}}^n_{h\tau}, \underline{\underline{\epsilon}}(\underline{v})) = 0$ inside the integral to conclude. For the first term we have, for a.e. $t \in (0, t_F)$,

$$|\mathfrak{T}_1(t)| = \left|\sum_{T\in\mathcal{T}^n_h} (\underline{f}^n + \underline{\nabla}\cdot\underline{\underline{\theta}}^n_h, (\underline{v} - \Pi_{K,T}\underline{v})(t))_T\right| \le \sum_{T\in\mathcal{T}^n_h} \eta^n_{R,T,U} E\|\underline{\underline{\epsilon}}(\underline{v})(t)\|_T,$$

where we have used (3.18a) to insert $\Pi_{K,T}\underline{v}$ inside the integral and (2.9) to conclude. For the second term, using the Cauchy–Schwarz inequality readily yields

$$|\mathfrak{T}_2(t)| \le \sum_{T\in\mathcal{T}^n_h} \|\underline{\underline{\theta}}^n_h - \underline{\underline{\theta}}(\underline{u}_{h\tau}, p_{h\tau})(t)\|_T \|\underline{\underline{\epsilon}}(\underline{v})(t)\|_T = \sum_{T\in\mathcal{T}^n_h} \eta^n_{F,T,U}(t) E\|\underline{\underline{\epsilon}}(\underline{v})(t)\|_T.$$

Inserting these results into (4.8) and applying the Cauchy-Schwarz inequality yields

$$|e_U(\underline{v})| \le \left(\int_{I_n} \sum_{T\in\mathcal{T}^n_h} (\eta^n_{R,T,U} + \eta^n_{F,T,U}(t))^2\mathrm{d}t\right)^{1/2} \times \left(\int_{I_n} (E\|\underline{\underline{\epsilon}}(\underline{v})(t)\|)^2\mathrm{d}t\right)^{1/2}.$$

Proceeding in a similar way for e^n_P using (3.18b) and Poincaré's inequality (2.6) in place of (3.18a) and (2.9), respectively, we obtain

$$|e_P(q)| \le \left(\int_{I_n} \sum_{T\in\mathcal{T}^n_h} (\eta^n_{R,T,P} + \eta^n_{F,T,P}(t))^2\mathrm{d}t\right)^{1/2} \times \left(\int_{I_n} (l^\star\|\underline{\nabla} q(t)\|)^2\mathrm{d}t\right)^{1/2}.$$

Combining these results and using again the Cauchy-Schwarz inequality yields

$$|e_U(\underline{v}) + e_P(q)| \leq \left(\int_{I_n} \sum_{T \in \mathcal{T}_h^n} (\eta_{R,T,U}^n + \eta_{F,T,U}^n(t))^2 + (\eta_{R,T,P}^n(t) + \eta_{F,T,P}^n(t))^2 \mathrm{d}t \right)^{1/2} \times \|(\underline{v}, q)\|_{X_n},$$

and passing to the supremum concludes the proof. □

Remark 4.2 (Data oscillation)**.** *Lemmas 3.2 and 3.5, and the mixed finite element space property* $\underline{\nabla} \cdot \underline{\underline{\Sigma}}_h^n(T) = \underline{V}_h^n(T)$ *and* $\nabla \cdot \underline{W}_h^n(T) = Q_h^n(T)$ *for any* $T \in \mathcal{T}_h^n$ *imply*

$$\eta_{R,T,U}^n = \frac{h_T}{\pi} \frac{\sqrt{2}}{\sin(\alpha_T/4)} E^{-1} \|\underline{f}^n - \Pi_{\underline{V}_h^n(T)} \underline{f}\|_T,$$
$$\eta_{R,T,P}^n = \frac{h_T}{\pi} \frac{t^\star}{l^\star} \|g^n - \partial_t^n(\nabla \cdot \underline{u}_{h\tau} + c_0 p_{h\tau}) - \Pi_{Q_h^n(T)}(g^n - \partial_t^n(\nabla \cdot \underline{u}_{h\tau} + c_0 p_{h\tau}))\|_T.$$

For the sake of convenience, we assumed the source terms $\underline{f}$ *and* g *to be piecewise constant in time. When this is not the case, an additional data time-oscillation term appears in the right-hand side of the bound* (4.7)*.*

Remark 4.3 (Other types of boundary conditions)**.** *If we consider inhomogeneous Neumann boundary conditions* $\underline{\underline{\theta}}(\underline{u}, p)\underline{n}_\Omega = \underline{\theta}_N$ *on* $\partial\Omega_{N,U} \subseteq \partial\Omega$ *and* $\underline{\phi}(p) \cdot \underline{n}_\Omega = \phi_N$ *on* $\partial\Omega_{N,P} \subseteq \partial\Omega$*, two more error estimators appear in* (4.7)*. The details of how they are obtained for the hydraulic part are shown in [17] and can be directly applied to linear elasticity. For each* $T \in \mathcal{T}_h^n$*, let* $\mathcal{E}_T^{N,U}$ *and* $\mathcal{E}_T^{N,P}$ *be the set of edges lying on* $\partial\Omega_{N,U}$ *and* $\partial\Omega_{N,P}$ *respectively, and let* $\underline{\underline{\theta}}_h^n$ *and* $\underline{\phi}_h^n$ *be the flux reconstructions of Remarks 3.3 and 3.6. Then we set*

$$\eta_{N,T,U}^n = \sum_{e \in \mathcal{E}_T^{N,U}} \frac{h_T (2h_e C_t)^{1/2}}{E \sin(\alpha_T/4) |T|^{1/2}} \|\underline{\underline{\theta}}_h^n \underline{n}_\Omega - \underline{\theta}_N\|_e,$$
$$\eta_{N,T,P}^n = \sum_{e \in \mathcal{E}_T^{N,P}} \frac{t^\star h_T (h_e C_t)^{1/2}}{l^\star |T|^{1/2}} \|\underline{\phi}_h^n \cdot \underline{n}_\Omega - \phi_N\|_e,$$

where $C_t \approx 0.77708$*, and* (4.7) *now reads*

$$e^n \leq \left(\int_{I_n} \sum_{T \in \mathcal{T}_h^n} \{(\eta_{R,T,U}^n + \eta_{F,T,U}^n(t) + \eta_{N,T,U}^n)^2 + (\eta_{R,T,P}^n + \eta_{F,T,P}^n(t) + \eta_{N,T,P}^n)^2\} \mathrm{d}t \right)^{1/2}.$$

To define a global-in-time a posteriori error estimate, we additionally define the *initial condition errors* $\eta_{\mathrm{IC},T,U}$ and $\eta_{\mathrm{IC},T,P}$ by setting

$$\eta_{\mathrm{IC},T,U} := \left(\frac{1}{2} E^{-1} t^\star \left(\underline{\underline{\sigma}}(\underline{u}_0 - \underline{u}_{h\tau}(\cdot, 0)), \underline{\underline{\epsilon}}(\underline{u}_0 - \underline{u}_{h\tau}(\cdot, 0)) \right)_T \right)^{1/2}, \tag{4.9a}$$
$$\eta_{\mathrm{IC},T,P} := \left(\frac{1}{2} E^{-1} (t^\star)^2 c_0 \left((p_0 - p_{h\tau}(\cdot, 0)), p_0 - p_{h\tau}(\cdot, 0) \right)_T \right)^{1/2}, \tag{4.9b}$$

and we set

$$e_{\mathrm{IC}} = \eta_{\mathrm{IC}} = \left(\sum_{T \in \mathcal{T}_h^0} \eta_{\mathrm{IC},T,U}^2 + \eta_{\mathrm{IC},T,P}^2 \right)^{1/2}. \tag{4.10}$$

We define the global error as

$$e := \|\mathcal{R}(\underline{u}_{h\tau}, p_{h\tau})\|_{X'} + e_{\mathrm{IC}}. \tag{4.11}$$

Corollary 4.4 (Global-in-time a posteriori error estimate)**.** *The following holds:*

$$e \le \left(\sum_{n=1}^{N} \int_{I_n} \sum_{T \in \mathcal{T}_h^n} \{ (\eta_{R,T,U}^n + \eta_{F,T,U}^n(t))^2 + (\eta_{R,T,P}^n + \eta_{F,T,P}^n(t))^2 \} \mathrm{d}t \right)^{1/2} + \eta_{\mathrm{IC}}. \tag{4.12}$$

Proof. For each $1 \le n \le N$, let $\xi_n \in X$ be the Riesz-representative of $J_n : X_n \to \mathbb{R}$ with $J_n(\underline{v}, q) = \int_{I_n} \mathcal{B}((\underline{u} - \underline{u}_{h\tau}, p - p_{h\tau}), (\underline{v}, q))\mathrm{d}t$. Then the function $\xi \in X$ defined by $\xi_{|I_n} := \xi_n$ will be the Riesz-representative of $J : X \to \mathbb{R}$ with $(\underline{v}, q) \mapsto \int_0^{t_F} \mathcal{B}((\underline{u} - \underline{u}_{h\tau}, p - p_{h\tau}), (\underline{v}, q))\mathrm{d}t$, so that

$$\|\mathcal{R}(\underline{u}_{h\tau}, p_{h\tau})\|_{X'}^2 = \|J\|_{X'}^2 = \|\xi\|_X^2 = \sum_{n=1}^{N} \|\xi_n\|_{X_n}^2 = \sum_{n=1}^{N} \|J_n\|_{X_n'}^2 = \sum_{n=1}^{N} (e^n)^2. \tag{4.13}$$

Inserting this result into (4.11) and applying Theorem 4.1 concludes the proof. □

4.2 Distinguishing the space and time error components

The goal of this section is to elaborate the error estimate (4.7) so as to distinguish the error components resulting from the spatial and the temporal discretization. This is essential for the development of Algorithm 4.6 below, where the space mesh and the time step are chosen adaptively. Therefore, we add and subtract the discrete fluxes in the flux estimators (4.6) and apply the triangle inequality. We obtain, for all $T \in \mathcal{T}_h^n$, the following local *spatial and temporal discretization error estimators*:

$$\eta_{\mathrm{sp},T,U}^n := \eta_{R,T,U}^n + E^{-1} \|\underline{\underline{\theta}}_h^n - \underline{\underline{\theta}}(\underline{u}_h^n, p_h^n)\|_T, \tag{4.14a}$$

$$\eta_{\mathrm{sp},T,P}^n := \eta_{R,T,P}^n + \frac{t^\star}{l^\star} \|\underline{\phi}_h^n - \underline{\phi}(p_h^n)\|_T, \tag{4.14b}$$

$$\eta_{\mathrm{tm},T,U}^n(t) := E^{-1} \|\underline{\underline{\theta}}(\underline{u}_h^n, p_h^n) - \underline{\underline{\theta}}(\underline{u}_{h\tau}, p_{h\tau})(t)\|_T, \tag{4.14c}$$

$$\eta_{\mathrm{tm},T,P}^n(t) := \frac{t^\star}{l^\star} \|\underline{\phi}(p_h^n) - \underline{\phi}(p_{h\tau})(t)\|_T. \tag{4.14d}$$

For each of these local estimators we can define a global version by setting

$$\eta_{\bullet,\{U,P\}}^n(t) := \left(2 \int_{I_n} \sum_{T \in \mathcal{T}_h^n} \left(\eta_{\bullet,T,\{U,P\}}^n(t) \right)^2 \mathrm{d}t \right)^{1/2}. \tag{4.15}$$

Inserting them into (4.7) and applying the triangle inequality yields the following result.

Theorem 4.5 (A posteriori error estimate distinguishing the error components)**.** *Let $1 \le n \le N$. Let $(\underline{u}, p)$ be the weak solution of (2.4) and let $(\underline{u}_{h\tau}, p_{h\tau}) \in Y^n$ be the discrete solution of (2.11). Let $\underline{\underline{\theta}}_h^n$, $\underline{\phi}_h^n$ be the equilibrated fluxes of Construction 3.8. Then the following holds for the error e^n defined by (4.3) with estimators defined by (4.14) and (4.15):*

$$e^n \le \eta_{\mathrm{sp},U}^n + \eta_{\mathrm{sp},P}^n + \eta_{\mathrm{tm},U}^n + \eta_{\mathrm{tm},P}^n. \tag{4.16}$$

4.3 Adaptive algorithm

Based on the error estimate of Theorem 4.5, we propose an adaptive algorithm where the mesh size and time step are locally adapted. The idea is to compare the estimators for the two error sources with each other in order to concentrate the computational effort on reducing the dominant one. Thus, both the spatial mesh and the time step are adjusted until space and time discretization contribute nearly equally to the overall error. For this purpose, let $\Gamma_{\mathrm{tm}} > 1 > \gamma_{\mathrm{tm}} > 0$ be user-given weights and crit^n, for all $0 \leq n \leq N$, a chosen threshold that the error on the time interval I_n should not exceed. For each of the considered error sources we define the corresponding estimator as $\eta_\bullet := \eta_{\bullet,U} + \eta_{\bullet,P}$, so that (4.16) becomes

$$e^n \leq \eta_{\mathrm{sp}}^n + \eta_{\mathrm{tm}}^n \tag{4.17}$$

Algorithm 4.6 (Adaptive algorithm)**.**

1. **Initialisation**
   (a) Choose an initial triangulation $\mathcal{T}_h^0$, an initial time step τ_0, and set $t^0 := 0$
   (b) **Initial mesh adaptation loop**
   - Calculate $\eta_{\mathrm{IC},U}$ and $\eta_{\mathrm{IC,P}}$
   - Refine or coarsen the mesh $\mathcal{T}_h^0$ such that the local initial condition error estimators $\eta_{\mathrm{IC},T,\bullet}$ are distributed equally

   End of the loop if $\eta_{\mathrm{IC}} \leq \mathrm{crit}^0$
2. **Time loop**
   (a) Set $n := n + 1$, $\mathcal{T}_h^n := \mathcal{T}_h^{n-1}$, and $\tau_n := \tau_{n-1}$
   (b) Calculate $(\underline{u}_h^n, p_h^n)$ and the estimators η_{sp}^n and η_{tm}^n
   (c) **Space refinement loop**
      i. **Space and time error balancing loop**
         A. if $\gamma_{\mathrm{tm}}\eta_{\mathrm{sp}}^n > \eta_{\mathrm{tm}}^n$: Set $\tau_n := 2\tau_n$
         B. if $\Gamma_{\mathrm{tm}}\eta_{\mathrm{sp}}^n < \eta_{\mathrm{tm}}^n$: Set $\tau_n := \frac{1}{2}\tau_n$

         End of the space-time error balancing loop if

$$\gamma_{\mathrm{tm}}\eta_{\mathrm{sp}}^n \leq \eta_{\mathrm{tm}}^n \leq \Gamma_{\mathrm{tm}}\eta_{\mathrm{sp}}^n \qquad \text{or} \qquad \tau_n \leq \tau_{\min}$$

      ii. Refine or coarsen the mesh $\mathcal{T}_h^n$ such that the local spatial error estimators $\eta_{\mathrm{sp},T}^n$ are distributed equally

   End of the space refinement loop if

$$\eta_{\mathrm{sp}}^n + \eta_{\mathrm{tm}}^n \leq \mathrm{crit}^n \tag{4.18}$$

   End of the time loop if $t^n \geq t_F$

Owing to (4.11), (4.13), (4.17) and (4.18) the obtained discrete solution satisfies

$$e \leq \left(\sum_{n=1}^{N} (\mathrm{crit}^{\mathrm{n}})^2 \right)^{1/2} + \mathrm{crit}^0. \tag{4.19}$$

In order to keep computational costs in the algorithm low, the initial mesh and time step should be chosen in a way that they match the criteria crit^0 and crit^1. This can be achieved by performing only one time step before running the whole computation, and by modifying the initial discretization if they do not.

5 Numerical results

In this section we illustrate numerically our theoretical results on four test cases. For all tests we use the Taylor–Hood finite elements (2.10) with $k = 1$ and Construction 3.8 with $l = 0$ and $m = 1$. In the first two test cases, analytical solutions are known; the first one is a purely elastic, stationary problem and the second one a Biot's poro-elasticity problem. We analyze the convergence rates of the error estimators and compare them to those of an energy-type norm of the analytical error. The third test is the quarter five-spot problem, where we compare the results of the adaptive algorithm to a "standard" solution with fixed mesh and time steps. In the fourth test, the excavation of two parallel tunnels is simulated. It shows an industrial application of the error estimators used for remeshing and again compares the performance of Algorithm 4.6 to a standard resolution.

5.1 Purely mechanical analytical test

For this stationary, purely mechanical test we consider the mode I loading of a cracked plate, corresponding to pure tension at the top and the bottom applied at the infinity. Following [42], an analytical solution around the crack tip is given by

$$\underline{u}(r,\theta) = \frac{1+\nu}{E\sqrt{2\pi}} \sqrt{r} \begin{pmatrix} -\cos(\frac{\theta}{2})(3-4\nu-\cos(\theta)) \\ \sin(\frac{\theta}{2})(3-4\nu-\cos(\theta)) \end{pmatrix}, \tag{5.1}$$

leading to a singularity of the stress tensor at the crack tip. For our test, we restrain ourselves to the domain $\Omega = (-\frac{1}{2}, \frac{1}{2}) \times (-\frac{1}{2}, \frac{1}{2})$ with a straight crack from $(-\frac{1}{2}, 0)$ (cf. Figure 6), and impose the analytical solution (5.1) as Dirichlet boundary condition on $\partial\Omega$ and the crack faces to obtain the discrete solution $\underline{u}_h$. The Young modulus and the Poisson ratio are set to $E = 1$ and $\nu = 0$, leading to the Lamé parameters $\mu = 0.5$ and $\lambda = 0$. Since in this purely mechanical

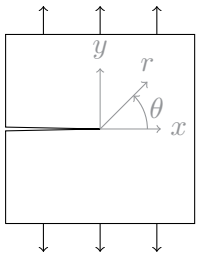

Figure 6: Loading of a cracked plate

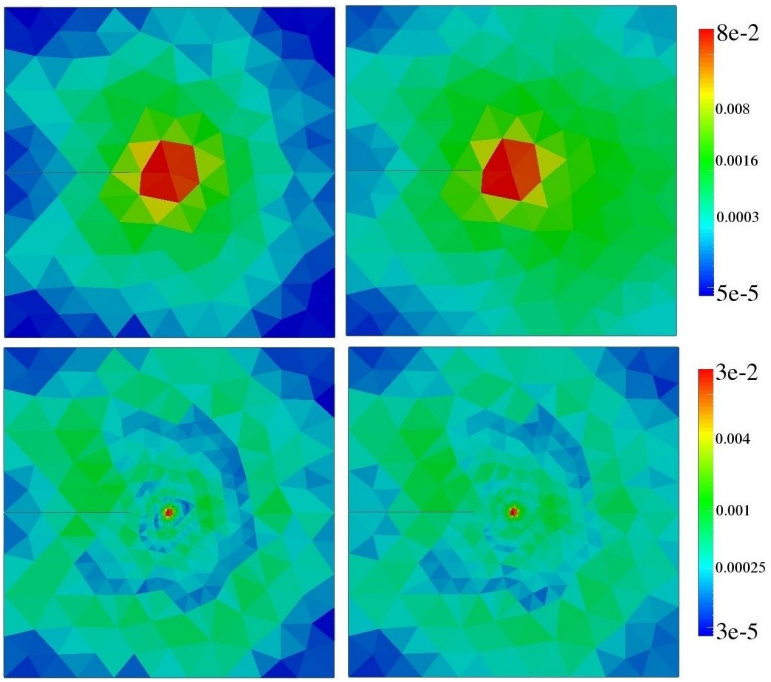

Figure 7: Error estimation (left) and analytical error (right) on an initial mesh and after three mesh refinements

test case there is no need for nondimensionalization, we omit the scaling factor E^{-1} in the error estimators. Figure 7 compares the distribution of the error estimators and the analytical error measured in the energy norm $\|\underline{u} - \underline{u}_h\|_{\text{en}} = a(\underline{u} - \underline{u}_h, \underline{u} - \underline{u}_h)^{1/2}$. Besides detecting the dominating error at the crack tip due to the singularity of $\underline{\underline{\sigma}}(\underline{u})$, the error estimators reflect the distribution of the analytical error in the whole domain, as can be seen in the lower panel for the finer mesh.

5.2 Poro-elastic analytical test

Let $\Omega = (0,1)\times(0,1)$. Following [7,18], we consider the analytical solution of Biot's consolidation problem (1.1)

$$\underline{u}(t,x,y) = \cos(-\pi t)\begin{pmatrix}\cos(\pi x)\sin(\pi y)\\ \sin(\pi x)\cos(\pi y)\end{pmatrix}, \quad p(t,x,y) = \sin(-\pi t)\sin(\pi x)\sin(\pi y),$$

with $\kappa = 1$, $c_0 = 0$, and the Lamé coefficients $\mu = \lambda = 0.4$, yielding a Young modulus $E = 1$ and a Poisson ratio $\nu = 0.25$. The resulting source terms are given by

$$\underline{f}(t,x,y) = (2.4\pi^2\cos(-\pi t) + \pi\sin(-\pi t))\begin{pmatrix}\cos(\pi x)\sin(\pi y)\\ \sin(\pi x)\cos(\pi y)\end{pmatrix},$$

and $g = 0$.

To evaluate convergence rates under space or time uniform refinement, we measure the analytical error in the energy norm

$$|||(v,q)|||^2_{\text{en}} = \int_0^{t_F} \mathcal{B}((\underline{v},q),(t^\star\partial_t\underline{v},q))\mathrm{d}t = \frac{1}{2}t^\star\left(a(\underline{v},\underline{v})(t_F) - a(\underline{v},\underline{v})(t_0)\right) + t^\star\int_0^{t_F} d(q,q)\mathrm{d}t, \quad (5.2)$$

h^{-1}	$\eta_{\mathrm{sp},U}$		$\eta_{\mathrm{sp},P}$		$\|\underline{u}-\underline{u}_{h\tau}\|_U$		$\|p-p_{h\tau}\|_P$		e_{en}	I_{eff}
4	3.45e-2	—	1.58	—	3.44e-2	—	4.67e-1	—	5.12e-1	3.15
8	8.13e-3	2.09	7.62e-1	1.05	8.11e-3	2.08	2.33e-1	1.07	2.46e-1	3.14
16	1.96e-3	2.05	3.76e-1	1.02	2.00e-3	2.02	1.10e-1	1.02	1.21e-1	4.04
32	4.85e-4	2.01	1.87e-1	1.01	9.03e-4	1.15	5.46e-2	1.01	6.03e-2	3.16

Table 1: Error estimators and analytical errors under space refinement with $t_F = 0.5$, $\tau =$ 5e-5

τ^{-1}	$\eta_{\mathrm{tm},U}$		$\eta_{\mathrm{tm},P}$		$\|\underline{u}-\underline{u}_{h\tau}\|_U$		$\|p-p_{h\tau}\|_P$		e_{en}	I_{eff}
4	4.73e-1	—	2.54e-1	—	1.96e-1	—	2.09e-1	—	2.32e-1	3.34
8	2.40e-1	0.78	1.40e-1	0.86	9.88e-2	1.00	1.14e-1	0.87	1.27e-1	3.35
16	1.20e-1	1.00	7.31e-2	0.94	4.94e-2	1.00	6.03e-2	0.92	6.94e-2	3.46
32	6.00e-2	1.00	3.74e-2	0.97	2.47e-2	1.00	3.17e-2	0.93	3.85e-2	3.76

Table 2: Error estimators and analytical errors under time refinement with $t_F = 0.5$, $h = 1/128$

and the mechanical and hydraulic parts separately in the following norms:

$$\|\underline{v}\|_U^2 = \int_0^{t_F} a(\underline{v},\underline{v})\mathrm{d}t \quad \text{and} \quad \|q\|_P^2 = \int_0^{t_F} d(q,q)\mathrm{d}t. \tag{5.3}$$

where in this dimensionless test, the nondimensionalization parameters $t^\star$ and $l^\star$ are both equal to one, and we also omit the factor E.

Tables 1 and 2 compare the convergence rates under space and time refinement of the corresponding error estimators to the analytical error in the norms defined by (5.2) and (5.3). The last column shows the effectivity index defined by

$$I_{\mathrm{eff}} := \frac{\eta_{\mathrm{sp},U} + \eta_{\mathrm{sp},P} + \eta_{\mathrm{tm},U} + \eta_{\mathrm{tm},P}}{|||(\underline{u}-\underline{u}_{h\tau}, p-p_{h\tau})|||_{\mathrm{en}}}. \tag{5.4}$$

For both the spatial and the temporal refinement, we obtain the expected convergence rates of the Taylor–Hood finite element method (2.10) with $k = 1$, and a backward Euler scheme in time. The last value of the analytical mechanical error under space refinement is due to the error in time discretization which starts playing a role for the finest mesh. We observe that the orders of magnitude of the mechanical and hydraulic part are comparable in this test, and that the effectivity index is dominated by the hydraulic part under space refinement, and by the mechanical part under time refinement.

5.3 Quarter five-spot problem

In this standard configuration considered in petroleum engineering, the injection of water at the center of a square domain and the production at the four corners is simulated on a quarter of the domain. In our test, this quarter is a square of 100m side length, divided into two parts with different mobilities; a circle around the injection point of radius 50m with $\kappa = 8{\cdot}10^{-9}\mathrm{m}^2\mathrm{Pa}^{-1}\mathrm{s}^{-1}$, and $\kappa = 10^{-9}\mathrm{m}^2\mathrm{Pa}^{-1}\mathrm{s}^{-1}$ in the rest of the domain. The Young modulus and the Poisson ratio are given by $E = 10^9\mathrm{Pa}$, $\nu = 0.3$, and we set $c_0 = 0$. The initial state is given by $\underline{\theta}_0 = \underline{0}$, $\underline{\phi}_0 = \underline{0}$ and $p_0 = 10^5\mathrm{Pa}$. During the computation time of 30 days, we set $p = p_0$ in the top right corner and $p = 4 \cdot 10^5\mathrm{Pa}$ in the bottom left corner, simulating the production and the injection respectively. The nondimensionalization parameters are $l^\star = 140\mathrm{m}$ and $t^\star = 1\mathrm{h}$. The problem is dominated by hydraulic processes.

	# space-time unknowns	# iterations	η_{sp}	η_{tm}	$\eta_{\text{sp}}+\eta_{\text{tm}}$
reference	13,754,520	120	0.204	0.315	0.519
equivalent	973,620	45	1.14	1.54	2.68
adaptive	846,174	71	0.462	0.507	0.969

Table 3: The three computations in our test for the quarter five-spot problem

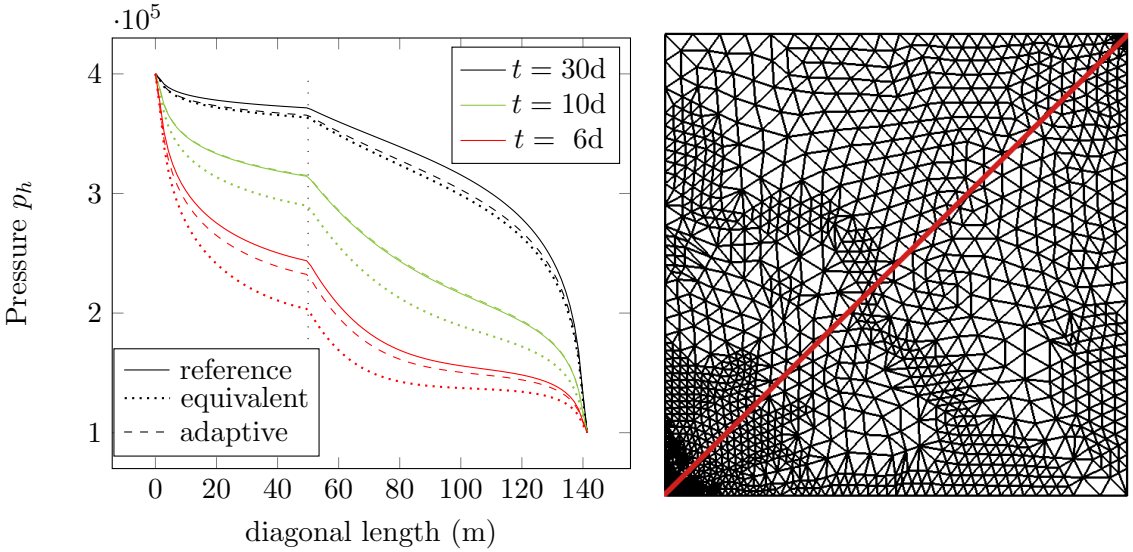

Figure 8: Left: Comparison of the pressure in the quarter five-spot problem along the diagonal between the three algorithms in Table 3. Right: An adapted mesh at time $t = 10$ days

We use Algorithm 4.6 to perform space-time adaptivity. We start with an initial mesh of 10,638 vertices and with an initial time step of $\tau_0 = 12$h. For the space-time error balancing, we set $\gamma_{tm} = 0.8$ and $\Gamma_{tm} = 1.3$ and fix the error limit for each time step to $\text{crit}^n = 0.005\tau_n$. We compare the performance of the adaptive algorithm to two static computations (i.e. with fixed meshes and time steps), one, called equivalent, where the discretization is chosen in a way to have approximately the same number of space-time unknowns as in the adaptive algorithm, and one where the discretization is very fine, so its solution can be taken as a reference solution. Table 3 compares the number of space-time unknowns and performed iterations (i.e. the number of time steps, counting repetitions in the adaptive algorithm), and the values of the error estimators of the three computations.

The left graphic in Figure 8 shows the discrete pressure along the diagonal going from the bottom left to the top right of the domain (as indicated in the right graphic) at three different times obtained by the static computations (solid and dotted lines) and the adaptive algorithm (dashed lines). The loosely dotted vertical line marks the edge between the two parts of Ω with different permeabilities. At each of these times, the discrete solution of the adaptive algorithm is closer to the reference solution than the equivalent computation using a fixed mesh and time step. At the last time step, all the results get closer as the solution converges in time to a constant state.

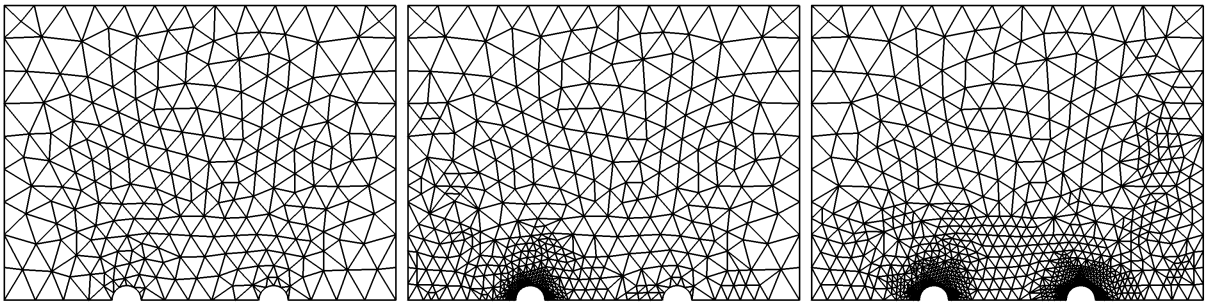

Figure 9: Initial mesh (left) and meshes at the end of the first (center) and the second (right) excavation in the adaptive algorithm

5.4 Excavation damage test

In the context of the conception of a radioactive waste repository site, the excavation of tunnels destined to contain waste packages is numerically simulated. The domain Ω is a 80m $\times$ 60m quadrilateral, vertical cutout of the rock, in which two galleries are digged time-delayed in the z-direction, first left, then right. Both excavations take 17.4 days ($1.5 \cdot 10^6$s) and the second one starts 11.6 days (10^6s) after the end of the first one. For both excavations we first calculate the initial total equilibrium of the hole-free geometry. Then the digging is simulated by linearly decreasing boundary conditions on the tunnel (convergence confinement method). These are of Neumann type for the mechanical part and of Dirichlet type for the hydraulic part and start with the total stress measured at the equilibrium state and the pressure $p_0 = 4.7$MPa. Homogeneous Dirichlet boundary conditions for the y-component of the displacement and $p = p_0$ are imposed on the bottom of Ω (except for the tunnel parts), while on the top, the left and the right sides of Ω, we set $\underline{\underline{\theta}}\underline{n} = \underline{\underline{\theta}}_{\mathrm{ref}}\underline{n}$ with $(\underline{\underline{\theta}}_{\mathrm{ref},xx}, \underline{\underline{\theta}}_{\mathrm{ref},yy}, \underline{\underline{\theta}}_{\mathrm{ref},xy}) := (-11\mathrm{MPa}, -15.4\mathrm{MPa}, 0)$ and $p = p_0$. These boundary conditions have to be taken into account for the stress reconstruction (cf. Remark 3.6) and the a posteriori error estimate (cf. Remark 4.3). The initial fluxes are given by $\underline{\underline{\theta}}_0 = \underline{\underline{\theta}}_{\mathrm{ref}}$ and $\underline{\phi}_0 = \underline{0}$, while the initial pressure is p_0. The parameters describing the rock are the Young modulus $E = 5800$MPa, the Poisson ratio $\nu = 0.3$, the specific storage coefficient $c_0 = 0$, and the hydraulic mobility $\kappa = 10^{-13}\mathrm{m}^2\mathrm{Pa}^{-1}\mathrm{s}^{-1}$. For the nondimensionalization of the problem, we used, along with E, the parameters $t^\star = 1$h and $l^\star = 100$m.

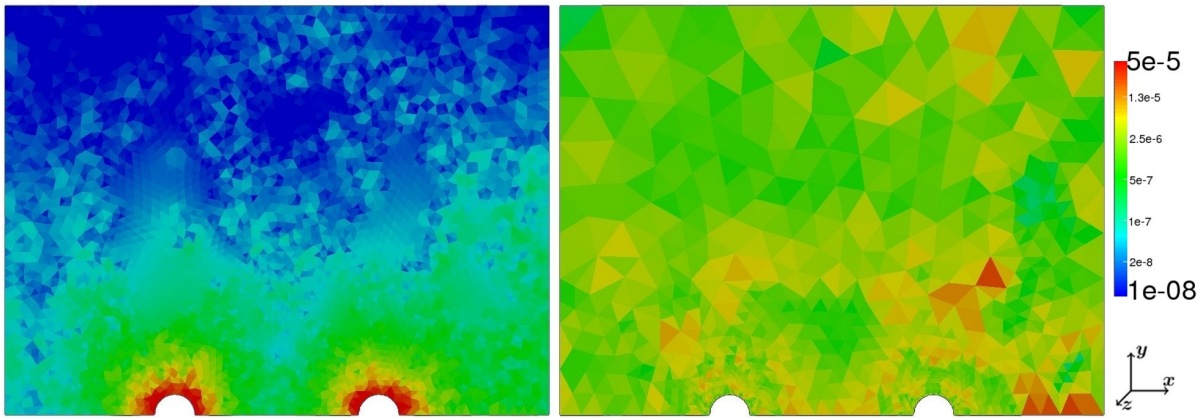

Figure 10: Spatial discretization error estimators at t_F on a fixed mesh (left, 29,275 dofs) and on the last mesh of an adaptive algorithm (right, 15,064 dofs)

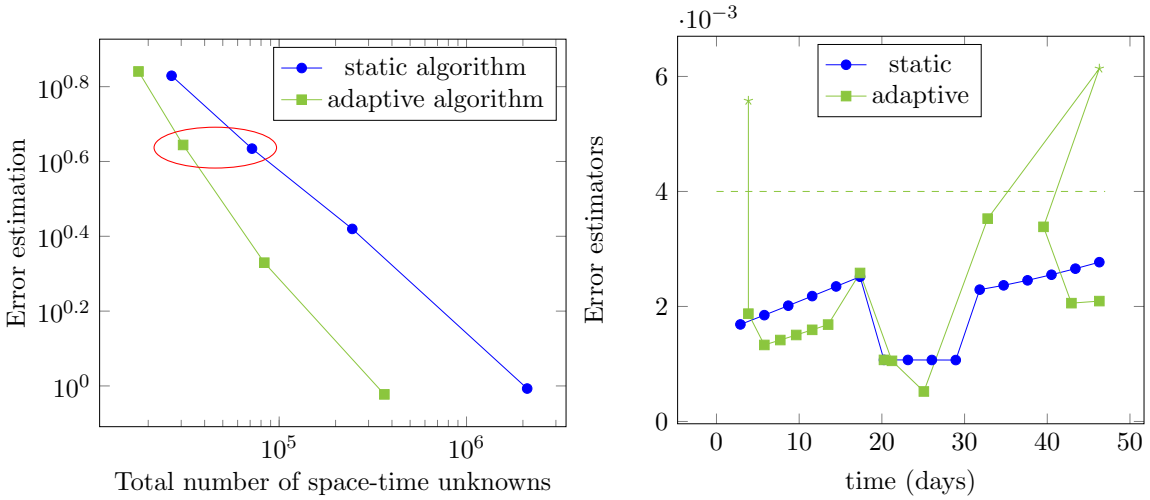

Figure 11: Comparison between a static algorithm with fixed mesh and time step and the adaptive algorithm 4.6 for the excavation damage test

The performance of Algorithm 4.6 is tested on four different initial meshes with $\text{crit}^n = 7 \cdot 10^{-3}\tau_n$ for the coarsest one and, with the mesh getting finer, $\text{crit}^n = 4 \cdot 10^{-3}\tau_n$, $\text{crit}^n = 2 \cdot 10^{-3}\tau_n$ and $\text{crit}^n = 1 \cdot 10^{-3}\tau_n$. In all the calculations we fix $\gamma_{\text{tm}} = 0.8$, $\Gamma_{\text{tm}} = 1.5$ and $\tau_0 = 3.9\text{d}$. Figure 9 illustrates the evolution of the second coarsest mesh with $\text{crit}^n = 4 \cdot 10^{-3}\tau_n$. During the first excavation, the refinement takes only place around the left tunnel, whereas the area around the right tunnel is only refined after the beginning of the second excavation. The calculations resulting from the adaptive algorithm are compared to calculations with fixed meshes and time steps. Each of these meshes is slightly finer around the tunnels than in the rest of Ω, and the time steps are chosen in a way that $\eta_{\text{sp}} \approx \eta_{\text{tm}}$. Figure 10 compares the spatial discretization error estimators at the final time t_F of the static algorithm to those of the adaptive algorithm, which are much more evenly distributed over the domain. Furthermore, the left graphic in Figure 11 shows that in our test, the use of the adaptive algorithm reduces the number of space-time-unknowns for a similar value of the error estimator.

In the right graphic of Figure 11, we plot the evolution of the error estimators in the two computations circled in the left graphic. Each mark stands for an iteration and shows the error estimate e^n of the current time interval divided by τ_n. For the plain algorithm, an iteration is equal to a time step. The adaptive algorithm recalculates the solution at a time step whenever the error estimate lies over crit^n (illustrated by the dashed line) by refining τ_n or the mesh (or both). Thus, only the square shaped points in the graphic contribute to the overall error estimate. In the consolidation phase between the two excavations (from $t = 17.4$ days to $t = 29$ days), the mesh is slightly coarsened and the time step considerably increased, since the dominating error source in this phase is the spatial discretization.

5.5 Conclusion

The analytical test cases show that the distribution and convergence rates of our error estimators reflect those of the analytical error. The efficiency of Algorithm 4.6 has been illustrated in industrial tests, where the number of space-time unknowns is considerably decreased for a comparable overall error estimate. We also observe that the price for computing the flux reconstructions can be substantially reduced by pre-processing, a task that is fully parallelizable.

As shown in the first test, the stress reconstruction and a posteriori estimate presented in this work are directly applicable to pure linear elasticity problems. The second test shows that the presented error estimate also delivers sharp bounds (as reflected by moderate effectivity indices) of more accessible error measures computed using energy-type norms. In the third and fourth tests, comparing the proportions of the estimators for the hydraulic and the mechanical parts reflects the physical properties of the problem: in the quarter five-spot test, the dominating estimators are those for the hydraulic part; for the excavation damage test, they are approximately of the same order of magnitude, with the mechanical estimator dominating in regions of stress concentration.

Acknowledgements

The work of D. A. Di Pietro was supported by ANR grant HHOMM (ANR-15-CE40-0005)

References

References

[1] M. Ainsworth and J. T. Oden. A posteriori error estimation in finite element analysis. *Pure and Applied Mathematics (New York), Wiley-Interscience [John Wiley & Sons], New York*, 2000.

[2] M. Ainsworth and R. Rankin. Guaranteed computable error bounds for conforming and nonconforming finite element analysis in planar elasticity. *Internat. J. Numer. Methods Engrg*, 82:1114–1157, 2000.

[3] D. N. Arnold, G. Awanou, and R. Winther. Finite elements for symmetric tensors in three dimensions. *Math. Comp.*, 77:1229–1251, 2008.

[4] D. N. Arnold and R. Winther. Mixed finite elements for elasticity. *Numer. Math.*, 92:401–419, 2002.

[5] M. Bebendorf. A note on the Poincaré inequality for convex domains. *Z. Anal. Anwendungen*, 22:751–756, 2003.

[6] M. A. Biot. General theory of three-dimensional consolidation. *J. Appl. Phys.*, 12:155–169, 1941.

[7] D. Boffi, M. Botti, and D. A. Di Pietro. A nonconforming high-order method for the Biot problem on general meshes. *SIAM J. Sci. Comput.*, 38(3):A1508–A1537, 2016.

[8] D. Braess, V. Pillwein, and J. Schöberl. Equilibrated residual error estimates are p-robust. *Comput. Methods Appl. Mech. Engrg.*, 198:1189–1197, 2009.

[9] D. Braess and J. Schöberl. Equilibrated residual error estimator for edge elements. *Math. Comp.*, 77(262):651–672, 2008.

[10] L. Chamoin, P. Ladevèze, and F. Pled. An enhanced method with local energy minimization for the robust a posteriori construction of equilibrated stress field in finite element analysis. *Comput. Mech.*, 49:357–378, 2012.

[11] P. Destuynder and B. Métivet. Explicit error bounds in a conforming finite element method. *Math. Comput.*, 68(228):1379–1396, 1999.

[12] D. A. Di Pietro and A. Ern. A hybrid high-order locking-free method for linear elasticity on general meshes. *Comput. Meth. Appl. Mech. Engrg*, 283:1–21, 2015.

[13] D. A. Di Pietro, A. Ern, and J.-L. Guermond. Discontinuous Galerkin methods for anisotropic semi-definite diffusion with advection. *SIAM J. Numer. Anal.*, 46(2):805–831, 2008.

[14] D. A. Di Pietro, E. Flauraud, M. Vohralík, and S. Yousef. A posteriori error estimates, stopping criteria, and adaptivity for multiphase compositional Darcy flows in porous media. *J. Comput. Phys.*, 276:163–187, 2014.

[15] D. A. Di Pietro, M. Vohralík, and S. Yousef. An posteriori-based, fully adaptive algorithm for thermal multiphase compositional flows in porous media with adaptive mesh refinement. *Comput. and Math. with Appl.*, 68(12):2331–2347, 2014.

[16] D. A. Di Pietro, M. Vohralík, and S. Yousef. Adaptive regularization, linearization, and discretization and a posteriori error control for the two-phase Stefan problem. *Math. Comp*, 84(291):153–186, 2015.

[17] V. Dolejší, A. Ern, and M. Vohralík. *hp*–adaption driven by polynomial-degree-robust a posteriori error estimates for elliptic problems. *SIAM J. Sci. Comput.*, 38(5):A3220–A3246, 2016.

[18] A. Ern and S. Meunier. A posteriori error analysis of Euler-Galerkin approximations to coupled elliptic-parabolic problems. *ESAIM Math. Mod. Numer. Anal..*, 43:353–375, 2009.

[19] A. Ern and M. Vohralík. A posteriori error estimation based on potential and flux reconstruction for the heat equation. *SIAM J. Numer. Anal.*, 48(1):198–223, 2010.

[20] A. Ern and M. Vohralík. Adaptive inexact Newton methods with a posteriori stopping criteria for nonlinear diffusion PDEs. *SIAM J. Sci. Comput.*, 35(4):A1761–A1791, 2013.

[21] A. Ern and M. Vohralík. Polynomial-degree-robust a posteriori estimates in a unified setting for conforming, nonconforming, discontinuous Galerkin, and mixed discretizations. *SIAM J. Numer. Anal.*, 53(2):1058–1081, 2015.

[22] Kwang-Yeon Kim. Guaranteed a posteriori error estimator for mixed finite element methods of linear elasticity with weak stress symmetry. *SIAM J. Numer. Anal.*, 48:2364–2385, 2011.

[23] P. Ladevèze. *Comparaison de modèles de milieux continus*. PhD thesis, Université Pierre et Marie Curie (Paris 6), 1975.

[24] P. Ladevèze and D. Leguillon. Error estimate procedure in the finite element method and applications. *SIAM J. Numer. Anal.*, 20:485–509, 1983.

[25] P. Ladevèze, J. P. Pelle, and P. Rougeot. Error estimation and mesh optimization for classical finite elements. *Engrg. Comp.*, 8(1):69–80, 1991.

[26] R. Luce and B. I. Wohlmuth. A local a posteriori error estimator based on equilibrated fluxes. *SIAM J. Numer. Anal.*, 42:1394–1414, 2004.

[27] S. Meunier. *Analyse d'erreur a posteriori pour les couplages hydro-Mécaniques et mise en œuvre dans Code_Aster*. PhD thesis, École des Ponts ParisTech, 2007.

[28] M. A. Murad and A. F. D. Loula. Improved accuracy in finite element analysis of Biot's consolidation problem. *Comput. Meth. Appl. Mech. Engrg.*, 95:359–382, 1992.

[29] M. A. Murad and A. F. D. Loula. On stability and convergence of finite element analysis of Biot's consolidation problem. *Internat. J. Numer. Methods Engrg.*, 37:645–667, 1994.

[30] M. A. Murad, V. Thomée, and A. F. D. Loula. Asymptotic behaviour of semidiscrete finite-element approximations of Biot's consolidation problem. *SIAM J. Numer. Anal.*, 33(3):1065–1083, 1996.

[31] S. Nicaise, K. Witowski, and B. Wohlmuth. An a posteriori error estimator for the lamé equation based on H(div)-conforming stress approximations. *IMA J. Numer. Anal.*, 28:331–353, 2008.

[32] S. Ohnimus, E. Stein, and E. Walhorn. Local error estimates of FEM for displacements and stresses in linear elasticity by solving local Neumann problems. *Int. J. Numer. Meth. Engng.*, 52:727–746, 2001.

[33] P. J. Phillips and M. J. Wheeler. A coupling of mixed and continous Galerkin finite element methods for poroelasticity II: the discrete-in-time case. *Comput Geosci*, 11:145–158, 2007.

[34] W. Prager and J. L. Synge. Approximations in elasticity based on the concept of function space. *Quart. Appl. Math.*, 5:241–269, 1947.

[35] P. A. Raviart and J. M. Thomas. *A mixed finite element method for second order elliptic problems*, volume 606 of *Lecture Notes in Math.* Springer, 1975.

[36] S. I. Repin. *A posteriori estimates for partial differential equations*, volume 4 of *Radon Series on Computational and Applied Mathematics*. Walter de Gruyter GmbH & Co. KG, Berlin, 2008.

[37] R. S. Sandhu and E. L. Wilson. Finite element analysis of seepage in elastic media. *J. Engrg. Mech. Div. Amer. Soc. Civil. Engrg.*, 95:641–652, 1969.

[38] R. E. Showalter. Diffusion in poro-elastic media. *J. Math. Anal. Appl.*, 251:310–340, 2000.

[39] C. Taylor and P. Hood. A numerical solution of the Navier-Stokes equations using the finite element technique. *Comput. & Fluids*, 1:73–100, 1973.

[40] K. von Terzaghi. *Theoretical soil mechanics*. Wiley, New York, 1943.

[41] A. Ženíšek. The existence and uniqueness theorem in Biot's consolidation theory. *Aplikace Matematiky*, 29:194–211, 1984.

[42] M. Williams. On the stress distribution at the base of a stationary crack. *J. Appl. Mech.*, 24:109–114, 1957.

[43] Y. Yokoo, K. Yamagata, and H. Nagaoka. Finite element method applied to Biot's consolidation theory. *Soils and Foundations*, 11:29–46, 1971.